

Full length article

A phase-field model for hydride formation in polycrystalline metals: Application to δ -hydride in zirconium alloys

Tae Wook Heo^{a,*}, Kimberly B. Colas^{c,d}, Arthur T. Motta^{c,b}, Long-Qing Chen^b^a Materials Science Division, Lawrence Livermore National Laboratory, Livermore, CA 94550, USA^b Department of Materials Science and Engineering, The Pennsylvania State University, University Park, PA 16802, USA^c Department of Nuclear Engineering, The Pennsylvania State University, University Park, PA 16802, USA^d CEA/DEN/Service d'Etude des Matériaux Irradiés, CEA/Saclay, 91191 Gif-sur-Yvette Cedex, France

ARTICLE INFO

Article history:

Received 30 May 2019

Revised 21 August 2019

Accepted 24 September 2019

Available online 28 September 2019

Keywords:

Metal–hydrogen interactions

Hydride formation

Polycrystals

Zirconium hydrides

Phase-field model

ABSTRACT

We report a phase-field model for simulating metal hydride formation involving large volume expansion in single- and polycrystals. As an example, we consider δ -hydride formation in α -zirconium (Zr), which involves both displacive crystallographic structural change and hydrogen diffusion process. Thermodynamic Gibbs energy functions are extracted from the available thermodynamic database based on the sublattice model for the interstitial solid solutions. Solute–grain boundary interactions and inhomogeneous elasticity of polycrystals are taken into consideration within the context of diffuse-interface description. The stress-free transformation strains of multiple variants for *hcp*-Zr (α) to *fcc*-hydride (δ) transformation are derived based on the well-established orientation relationship between the α and δ phases as well as the corresponding temperature-dependent lattice parameters. In particular, to account for the large volume expansion, we introduced the *mixed* interfacial coherency concept between those phases—basal planes are coherent and prismatic planes are semi-coherent in computing the strain energy contribution to the thermodynamics. We analyzed the morphological characteristics of hydrides involving multiple structural variants and their interactions with grain boundaries. Moreover, our simulation study allows for the exploration of the possible hydride re-orientation mechanisms when precipitating under applied tensile load, taking into account the variation in the interfacial coherency between hydrides and matrix, their elastic interactions with the applied stress, as well as their morphology-dependent interactions with grain boundaries. The phase-field model presented here is generally applicable to hydride formation in any binary metal–hydrogen systems.

© 2019 Acta Materialia Inc. Published by Elsevier Ltd. All rights reserved.

1. Introduction

The metal–hydrogen interaction is an important topic in physical metallurgy owing to the diversity of its scientific issues as well as the duality of its roles in a broad range of practical applications. A representative example for the desirable incorporation of hydrogen in metals is hydrogen storage, *i.e.*, storing hydrogen in metals by forming simple or complex hydrides for the utility of its high-density clean energy [1–3]. On the other hand, the metal–hydrogen interaction may play a corrosive role, leading to mechanical failure of a metallic alloy due to the brittleness of the hydrides. For instance, the precipitation of a hydride rim may cause accelerated corrosion in Zr alloys [4]. Interestingly, the brittle hydrides can also be practically utilized to produce smaller

metallic particles via ball-milling and thermal decomposition processes (*e.g.*, Ti–H for producing small Ti particles [5,6]). To better utilize and control those positive and negative roles of hydrogen in metals, respectively, it is essential to establish a fundamental understanding of their thermodynamic and kinetic responses to the operating conditions. To that end, there have been a number of computational efforts in modeling metal–hydrogen interactions. These include fundamental computational thermodynamic calculations of metal–hydrogen systems [7], phenomenological kinetic modeling of hydrogenation [8], atomistic modeling and simulations of hydrogen diffusion [9–11], hydrogen–solid surface reaction [12–15], metal/hydride interfaces [16–18], and so forth.

However, in most cases, predicting the overall performance of operating metal–hydrogen interaction mechanisms is not straightforward due to the complicated multiphysics nature of these systems. In particular, hydride formation in metals, which is a key metal–hydrogen interaction, involves multiple physical, chemical, and materials processes, including adsorption of

* Corresponding author.

E-mail address: heo1@llnl.gov (T. Heo).

hydrogen-containing molecules, hydrogen diffusion, and phase transformation [1]. These processes are concurrent and inherently coupled, adding complexity to analyzing the hydride formation mechanisms. Moreover, the thermodynamics and kinetics of the processes are also strongly influenced by the associated microstructure of the parent metal and hydride precipitates [19,20]. Therefore, to better establish a fundamental mechanistic understanding of the coupled processes, it is necessary to devise a comprehensive modeling framework within which the relevant thermodynamic and kinetic factors, microstructural effects, and corresponding materials parameters are consistently assembled.

In this work, to develop an integrated mesoscale modeling platform for simulating hydride formation in metals, we employ the phase-field method [21–26] based on the diffuse-interface theory [27] using α -zirconium (Zr) as a model system. Zr alloys are widely utilized as structural materials in the nuclear energy industry for nuclear fuel cladding owing to their good mechanical properties, excellent high temperature corrosion resistance, and low neutron capture cross-section. However, in light water reactors, the Zr alloys claddings gradually pick up hydrogen generated by the corrosion reaction and water radiolysis, resulting in the formation of hydrides when the solubility of hydrogen in Zr is exceeded [28]. It is widely known that hydride formation during reactor operation degrades the mechanical behavior of the cladding, causing hydride embrittlement which can limit the lifetime of the component [29,30]. Moreover, the mechanical properties and performance of the Zr alloys are highly sensitive to the specific hydride microstructural configurations including shape, distribution, and orientation of the hydride particles. For example, when the hydrided cladding is subjected to high temperature (~ 300 – 400 °C for example) and applied loading during drying in preparation for dry storage or transportation of spent fuel, hydride platelets can dissolve and precipitate in a re-oriented direction from circumferential to radial orientations relative to the cladding tube geometry [31–33]. The re-oriented hydrides significantly degrade cladding ductility and can ultimately cause its mechanical failure since the fracture initiation and propagation can occur through the re-oriented radial hydrides. However, our understanding of the relevant microstructural mechanisms is still limited. Therefore, as these safety issues become increasingly important, predicting the hydride precipitate microstructures under the diverse processing and/or service conditions is a crucial step to ensuring long-term cladding stability against mechanical failure both during normal operation and long-term storage.

To model hydride formation and corresponding hydride microstructures, a number of phase-field models have been proposed. The first successful phase-field model for Zr hydride formation was proposed by Ma et al. focusing on nucleation and growth of the coherent γ -hydride and the effects of applied load [34]. This model was extended to simulate the formation of γ -hydride in bi-crystalline Zr [35,36] and to consider hydrogen diffusion and γ -hydride formation under a non-uniform stress field near a blunt notch [37]. To account for the plastic strains that accommodate the large volume expansion arising from hydride formation, Guo et al. developed an elastoplastic phase-field model [38] for simulating γ -hydride precipitation in Zr [39] and studied hydride formation in the presence of structural flaws such as cracks [40]. Thuinet et al. developed a phase-field model for investigating metastable ζ -hydrides focusing on the role of inhomogeneous elasticity [41,42]. Recently, more quantitative phase-field models were proposed to consider the temperature-dependent behaviors of hydride precipitation in Zr [43–45]. Incorporating the CALPHAD (CALculation of PHase Diagrams) database of the Zr–H binary system into the phase-field framework was also discussed [46]. More recently, Bair et al. applied the multiphase-field model [47] for considering metastable ζ and γ phases and studying their

roles in nucleation and growth of the stable δ hydride [48]. Han et al. reported their micromechanical phase-field model for investigating stacking structure formation of δ hydride precipitates in single crystal Zr, focusing on interfacial energy anisotropy and elastic interaction [49]. They proposed the hydride re-orientation mechanism based on local elastic energy-dependent nucleation sites near pre-existing hydride plates. Relevant review articles are currently available [28,50,51].

Here, we propose a comprehensive diffuse-interface mesoscale model that can investigate the underlying physics and associated mechanisms of hydride formation to predict hydride microstructure evolution in polycrystalline metals. We employ the δ hydride in the Zr–H system as a representative model system. We emphasize that the proposed model accounts for realistic thermodynamic energetics, mass transport kinetics, and several non-ideal factors focusing on metal/hydride interfacial coherency loss, hydrogen–grain boundary interaction, and hydride–grain boundary interaction.

2. Phase-field modeling framework

Our modeling framework is essentially the synthesis of the phase-field models for diffusional [52] and displacive [53] phase transformations in polycrystals, which include the physically-consistent descriptions for multivariant characteristics [54–59], inhomogeneous elasticity [60], solute–grain boundary interaction [61], and structural variant–grain boundary interaction [53]. In addition, our framework incorporates the available CALPHAD database in a thermodynamically consistent way. In this section, we present the essential modeling components that are systematically assembled within our diffuse-interface modeling framework.

2.1. Gradient thermodynamics

We chose the formation of hydrides in the Zr–H system as a representative example since this system exemplifies fundamental phase transformation mechanisms including both diffusional and displacive-types of transformations. We focus on the δ -hydride phase in α -Zr, which is the most commonly observed stable hydride phase formed in α -Zr alloys in service under practical reactor conditions [31, 62–64]. To model hydride formation within the phase-field context [21,27,65], we first define the necessary field variables that can properly describe the variation of the thermodynamic state and their kinetic pathways, which determine the microstructural features of the given material system in service. The formation of hydrides in a polycrystal involves three major coupled processes: (i) hydrogen diffusion, (ii) crystallographic structural transformation, and (iii) their interactions with grain boundaries. Accordingly, to account for these processes, three types of field variables are required: hydrogen composition (u), structural order parameter (η_{pg}), and grain order parameter (Ψ_g). For simplicity, we employ static grain order parameters, which are only necessary for describing interactions of structural variant and composition with grain boundaries. For the hydrogen composition, we use the atomic ratio of H to Zr for mathematical convenience in describing the thermodynamic model for an interstitial solid solution. Note that we use the two indices p and g for the structural order parameters to identify the structural variants in individual grains. Specifically, description of the α -Zr to δ -hydride transformation requires multiple structural order parameters. In particular, this involves an *hcp* to *fcc* crystallographic structural change [66], resulting in three distinct structural variants due to possible 3-fold symmetric shearing directions [49] as discussed in Section 2.2. Accordingly, we employ three structural order parameters (i.e., $p=1, 2, 3$) in each grain. Within the context of the diffuse-interface description [27], the total free energy functional is represented by the volume (V) integral

with the defined field variables (u , η_{pg} , Ψ_g) as the following:

$$F = \int_{\Omega} \left[f(u, \{\eta_{pg}\}) + \omega_{\eta} \cdot q(\{\eta_{pg}\}) - m_g \cdot g(\{\psi_g\}) \cdot u + \frac{\kappa_u}{2} (\nabla u)^2 + \sum_{p,g,i,j} \frac{\kappa_{\eta,ij}^g}{2} \nabla_i \eta_{pg} \nabla_j \eta_{pg} + e_{coh} \right] dV, \quad (1)$$

where f is the composition- and phase-dependent free energy density, ω_{η} is the energy barrier parameter, q is the Landau-type free energy density, m_g and g are the solute-grain boundary interaction parameter and potential topology function, respectively, κ_u and $\kappa_{\eta,ij}^g$ are the gradient energy coefficients for composition and order parameters, respectively, and e_{coh} is the coherency strain energy.

In fact, $(f + \omega_{\eta} \cdot q)$ represents the entire bulk free energy density of a transforming system. The energy barrier for the structural transformation is characterized by the parameter ω_{η} and the following Landau-type free energy:

$$q(\{\eta_{pg}\}) = \sum_{p,g} \eta_{pg}^2 \cdot (\eta_{pg} - 1)^2, \quad (2)$$

For the composition- and phase-dependent free energy part f , we adopt the thermodynamic description of the *Kim-Kim-Suzuki* (KKS) model [67]. Within this model, the interphase boundary is regarded as a mixture of the adjoining phases with equal chemical potentials. Therefore, the free energy density f and the composition (or atomic ratio) u ($=n_H/n_{Zr}$, where n_H , n_{Zr} are mole numbers of H and Zr atoms) of the mixture are written as:

$$f(u, \{\eta_{pg}\}) = h(\{\eta_{pg}\}) \cdot f_m^{\delta}(u_{\delta}) + (1 - h(\{\eta_{pg}\})) \cdot f_m^{\alpha}(u_{\alpha}), \quad (3)$$

$$u = h(\{\eta_{pg}\}) \cdot u_{\delta} + (1 - h(\{\eta_{pg}\})) \cdot u_{\alpha}, \quad (4)$$

where f_m^{δ} and f_m^{α} are the Gibbs energy functions for δ -hydride and α -Zr phases, respectively, and u_{δ} and u_{α} are the atomic ratios of H to Zr in the δ and α phases, respectively. For the interpolation function in Eqs. (3) and (4), we employed $h(\{\eta_{pg}\}) = \sum_{p,g} \eta_{pg}^3 (6\eta_{pg}^2 - 15\eta_{pg} + 10)$, which is widely used for the KKS model since it exhibits appropriate mathematical properties that do not cause unphysical artifacts: (i) $h(\eta = 0) = 1$, $h(\eta = 1) = 1$; (ii) $\partial h / \partial \eta|_{\eta=0,1} = 0$; (iii) $\partial^2 h / \partial \eta^2|_{\eta=0,1} = 0$. Eqs. (3) and (4) are coupled by the following equal chemical potential condition: $\partial f / \partial u = \partial f_m^{\delta}(u_{\delta}) / \partial u_{\delta} = \partial f_m^{\alpha}(u_{\alpha}) / \partial u_{\alpha}$. Note that this condition eliminates the unphysical interfacial potential [67] that usually limits the choice of interfacial thickness for large size scale phase-field simulations. Moreover, the thermodynamic driving force for the phase transformation can be clearly described by the free energy part f without the mathematically uncontrollable interfacial potential owing to the condition of equal chemical potential.

For the Gibbs energies for both α - and δ -phases of the Zr-H system, we adopt the *sublattice model* [68] to consistently implement the existing CALPHAD thermodynamic database for those interstitial solid solutions [69]. To describe the nonstoichiometric binary solid solution $Zr_a H_{b-\epsilon}$, we employ two sublattices for the Zr and H sites: $(Zr)_a (H, v_H)_b$, where the first sublattice sites are assumed to be fully occupied by Zr, and the second sublattice sites (*i.e.*, tetrahedral sites for both α and δ phases [66,69]) are assumed to be partially occupied by H (*i.e.*, occupied by H and vacant sites v_H). The subscripts a and b represent the numbers of moles of the sublattice sites per mole of the formula unit of the solid solution. Note that α phase is the interstitial solid solution of H in *hcp* Zr with a b/a site ratio 1, and δ -hydride is the hypo-stoichiometric *fcc* hydride with the b/a site ratio 2. Following the thermodynamic description of this model, we define the site fraction (y) of H in the second sublattice: $y = n_H^I / n_{sub}^I$, where n_H^I and n_{sub}^I are the (mole) numbers of the H atoms and total available sites, respectively, in the second sublattice. We then write the Gibbs energy function

$((G|H^{SER})_m^{\phi})$ per mole of alloy atoms with respect to the standard element reference (SER) for phase ϕ ($=\alpha$ or δ) as the following [69]:

$$(G|H^{SER})_m^{\phi} = G_m^{ref,\phi} + G_m^{id,\phi} + G_m^{xs,\phi}, \quad (5)$$

where $G_m^{ref,\phi}$ is the molar reference Gibbs energy of mixing, $G_m^{id,\phi}$ is the molar Gibbs energy of mixing for an ideal solution, and $G_m^{xs,\phi}$ is the excess Gibbs energy of mixing due to non-ideal solute-solvent and solute-solute interactions. Details of the individual Gibbs energy terms in Eq. (5) can be found in *Supplemental material S1*.

As discussed above, we introduced the atomic ratio of H to Zr ($u = n_H/n_{Zr} = X_H/X_{Zr}$, where n_H and n_{Zr} are mole numbers (X_H and X_{Zr} are mole fractions) of H and Zr atoms, respectively) to account for the hydrogen composition. It is important to note that this allows us to avoid the mathematical inconvenience that arises from the varying denominator with the changing interstitial hydrogen content when we use the usual definition of the composition X_H ($=n_H/(n_{Zr} + n_H)$, where n_H , n_{Zr} are mole numbers of H and Zr atoms). The conversion relation between y and u for $(Zr)_a (H, v_H)_b$ is given as $u = (b \cdot y)/a$. To consistently deal with the Gibbs energies across relevant phases with different stoichiometries using the variable u , we define the Gibbs energy per mole of Zr atoms (or formula unit of the hydride) instead of all alloy atoms. Therefore, the free energy functions in Eq. (3) can be written as:

$$f_m^{\phi} = \frac{1}{X_{Zr}} \cdot (G|H^{SER})_m^{\phi} = \frac{a + b \cdot y}{a} \cdot (G|H^{SER})_m^{\phi}. \quad (6)$$

We also note that this definition naturally permits using the derivatives of the free energy functions with respect to u in order to consistently define the relevant physical quantities. For example, the chemical potential of H can be written as:

$$\begin{aligned} \mu_H &= \frac{\partial (G|H^{SER})_m^{\phi}}{\partial X_H} = \frac{(1/X_{Zr}) \cdot \partial (G|H^{SER})_m^{\phi}}{(1/X_{Zr}) \cdot \partial X_H} \\ &= \frac{\partial \left[(G|H^{SER})_m^{\phi} / X_{Zr} \right]}{\partial [X_H/X_{Zr}]} = \frac{\partial f_m^{\phi}(u_{\phi})}{\partial u_{\phi}}. \end{aligned} \quad (7)$$

The third term ($-m_g \cdot g \cdot u$) in Eq. (1) denotes the thermodynamically-consistent solute-grain boundary interaction [52,61,70], where m_g is the interaction parameter determining the interaction strength between solute atoms (*i.e.*, hydrogen in this case) and a grain boundary, and g is the phenomenological function of grain order parameters $\{\psi_g\}$: $g(\{\psi_g\}) = \sum_g [-\frac{1}{2} \psi_g^2 + \frac{1}{4} \psi_g^4] + \gamma \sum_g \sum_{g' > g} \psi_g^2 \psi_{g'}^2 + \frac{1}{4}$, which determines the topology of the solute-grain boundary interaction potential that is non-zero only at the grain boundaries. For the gradient energy terms, in contrast to the original KKS model, we consider both gradients of composition ($\frac{\kappa_u}{2} (\nabla u)^2$) and order parameters ($\sum_{p,g,i,j} \frac{\kappa_{\eta,ij}^{pg}}{2} \nabla_i \eta_{pg} \nabla_j \eta_{pg}$), where κ_u and $\kappa_{\eta,ij}^{pg}$ are the gradient energy coefficients for composition and order parameters, respectively. We note here that the gradient energy for the composition may describe the possible isostructural phase separation mechanisms within the hydride phase. For example, as shown in Fig. S1(b), the free energy curve of the δ -hydride exhibits a double-well type feature, which incorporates the spinodal regime ($\partial^2 f_m^{\delta} / \partial u^2 \leq 0$). Therefore, our model can handle the spinodal decomposition of the hydride phase under certain conditions. The last term (e_{coh}) of Eq. (1) represents the coherency strain energy arising from the phase transformations that create phase boundaries. Detailed descriptions of the relevant physical factors can be found in the following section.

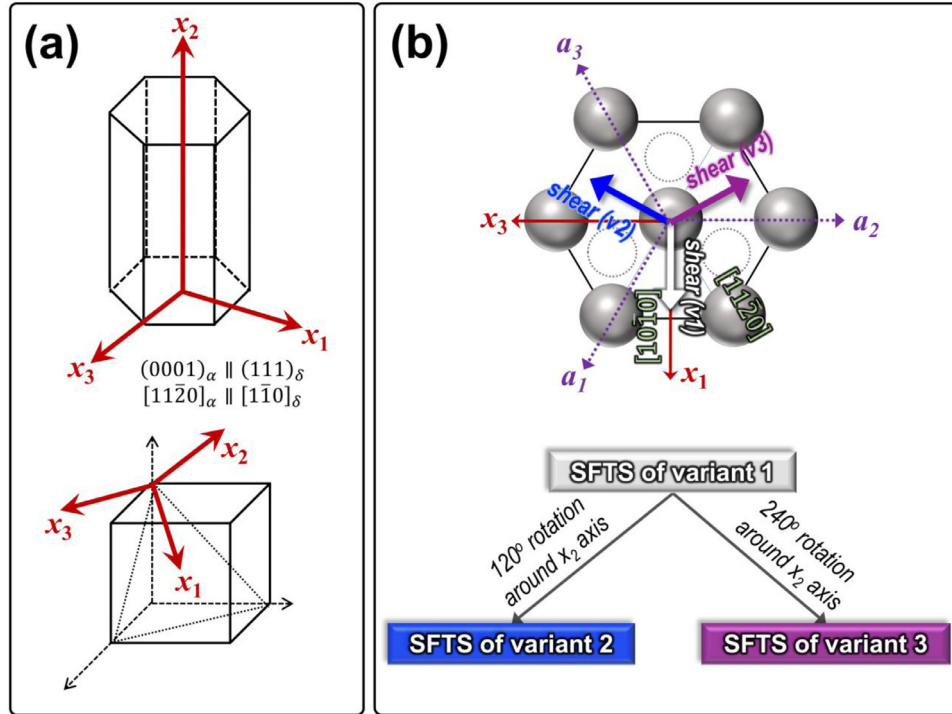


Fig. 1. (a) Defined coordinate system for hcp (top) and fcc (bottom) structures; and (b) Graphical description of three distinct structural variants (top) of the δ -hydride, and their 3-fold symmetric relationship (bottom).

2.2. Elastic interactions involving large volume expansion: mixed interfacial coherency

Hydride formation in a metal is associated with a large volume expansion due to the lower density of the hydride compared to the parent metal. Therefore, the associated mechanical stress and strain play a critical role in determining the phase transformation thermodynamics and kinetics. To compute the associated mechanical strain energy arising from the interfacial coherency along with the large volume expansion upon hydride formation within our modeling framework, the transformation strain should be properly derived within the context of the Khachaturyan microelasticity theory [71]. The formation of δ -hydrides in α -Zr is known to involve the hcp to fcc crystallographic structural transformation with the orientation relationship $\{0001\}_\alpha \parallel \{111\}_\delta$ and $(11\bar{2}0)_\alpha \parallel (1\bar{1}0)_\delta$ [72]. Accordingly, we define the $x_1 - x_2 - x_3$ coordinate system for hcp (top) and fcc (bottom) structures as described in Fig. 1(a) for the given orientation relationship. Note that the x_2 axis is parallel to the c -axis of the crystallographic coordinate system of the hcp structure. To systematically derive the corresponding stress-free transformation strain (SFTS) tensors, we decompose the transformation strain into three major components [73]: (I) shear along $\langle 10\bar{1}0 \rangle_\alpha$ directions to modify the stacking sequence for the hcp to fcc structural change; (II) isotropic lattice distortion in $\{0001\}_\alpha$ planes; (III) d -spacing change along $\langle 0001 \rangle_\alpha$ directions.

Note that this transformation produces three distinct structural variants [66] associated with the three possible shearing directions by which the fcc stacking sequence is established as shown in Fig. 1(b) (top). Since those three variants obey a 3-fold symmetric relationship, we may obtain the SFTSs for variants 2 and 3 by applying rotational symmetric operations to the SFTS for variant 1 (see Fig. 1(b) (bottom)). Therefore, we first derive the SFTS tensor for variant 1 by considering the corresponding strain components (I), (II), and (III). For mathematical convenience and consistency, we define the deformation gradient tensors for the individual strain components with respect to the $x_1 - x_2 - x_3$ coordinate

system defined in Fig. 1(a). For the component (I) for the variant 1, the deformation gradient tensor for the shear along x_1 direction is given as

$$\mathbf{F}_I(1) = \begin{pmatrix} 1 & \gamma & 0 \\ 0 & 1 & 0 \\ 0 & 0 & 1 \end{pmatrix}, \quad (8)$$

where $\gamma = (\frac{\sqrt{3}a_\alpha}{c_\alpha})/c_\alpha$ with the lattice parameters a_α and c_α of α -Zr. For the components (II), the isotropic lattice distortion in the $x_1 - x_3$ plane (i.e., basal plane) is described by the following deformation gradient:

$$\mathbf{F}_{II} = \begin{pmatrix} 1 + \beta & 0 & 0 \\ 0 & 1 & 0 \\ 0 & 0 & 1 + \beta \end{pmatrix}, \quad (9)$$

where $\beta = (\frac{1}{\sqrt{2}}a_\delta - a_\alpha)/a_\alpha$ is the lattice mismatch between α -Zr and δ -hydride along the $x_1 - x_3$ plane with the lattice parameters a_α and a_δ , respectively. With regard to the component (III), the d -spacing change along x_2 direction can be represented by

$$\mathbf{F}_{III} = \begin{pmatrix} 1 & 0 & 0 \\ 0 & 1 + \nu & 0 \\ 0 & 0 & 1 \end{pmatrix}, \quad (10)$$

where ν is the lattice mismatch along the x_2 direction. Note that the strain components (II) and (III) in Eqs. (9) and (10) are based on the fully coherent interface between α -Zr and δ -hydride. However, hydride formation involves large volume expansion, which usually leads to loss of the interfacial coherency due to the formation of dislocations which accommodate the volume change. This may partially contribute to the characterized peak broadening associated with the δ -hydride in the experimental synchrotron x-ray diffraction study [31,62], which can be caused by accumulated plastic and elastic strains. The possible impact of the interfacial coherency loss on the hydride microstructure will be discussed in Section 3.2 below. Therefore, to account for the corresponding coherency loss, we define the lattice mismatch ν

in Eq. (10) based on the *semi-coherent* interface assumption due to the dislocation array in the direction normal to the basal plane (i.e., along x_2 direction in our coordinate system) [74,75]:

$$\nu = \nu_{sem} = \left(m \cdot \left(\frac{2\sqrt{3}}{3} a_\delta \right) - n \cdot c_\alpha \right) / (n \cdot c_\alpha), \quad (11)$$

where m and n are positive integers that represent the lattice correspondence. In the limit of a perfectly coherent interface, the (m, n) pair becomes $(1, 1)$ with no interfacial dislocations, resulting in $\nu = \nu_{coh} = (2\sqrt{3}a_\delta - c_\alpha)/c_\alpha$. We note that although both m and n are integers in Eq. (11), ν can be simply parameterized by the rational number q ($= m/n$) (we define q as a *misfit parameter* hereafter). Note that the misfit parameter q can be characterized by the interfacial dislocation density.

For this *mixed* interfacial coherency case, we should assess whether the derived deformation gradient tensors properly contain the volumetric strain in order to correctly account for the transformation strain energy contribution involving the large volume change. Essentially, the deformation gradients for the SFTS should reproduce the same volumetric strain regardless of coherency loss, otherwise the total strain corresponding transformed volume cannot be appropriately considered when it is reintroduced into the matrix phase within the “Eshelby’s cycle” [76], which is the basis for the Khachaturyan microelasticity theory [71] employed in this study. However, the volumetric strain associated with the deformation gradient tensor in Eq. (10) is underestimated for the mixed coherency case since the strain component ν is merely reduced without proper consideration of the reduced amount of the strain. To remedy this error, we introduce the additional deformation gradient that incorporates the underestimated volume change assuming that this is equally distributed along the three orthogonal directions as the following:

$$\mathbf{F}_{vol} = \begin{pmatrix} 1 + \epsilon & 0 & 0 \\ 0 & 1 + \epsilon & 0 \\ 0 & 0 & 1 + \epsilon \end{pmatrix}, \quad (12)$$

where ϵ corresponds to the underestimated volume change element. To determine ϵ , we equate the volumetric strain for the mixed coherency case with the perfect coherency counterpart as a reference: $\epsilon_\nu = \det(\mathbf{F}_{III}^{coh} \cdot \mathbf{F}_{II} \cdot \mathbf{F}_I(1)) - 1 = \det(\mathbf{F}_{vol} \cdot \mathbf{F}_{III}^{sem} \cdot \mathbf{F}_{II} \cdot \mathbf{F}_I(1)) - 1$, where $\det(F)$ represents the determinant of the matrix F . This results in $\epsilon = (1 + (\nu_{coh} - \nu_{sem}) / (1 + \nu_{sem}))^{1/3} - 1$. By combining all the derived deformation gradient tensors, the SFTS for the variant 1 is written based on the finite strain formalism as the following:

$$\mathbf{E}^{000}(1) = (1/2) \cdot (\mathbf{C}_{tot}(1) - I), \quad (13)$$

where $\mathbf{C}_{tot}(1)$ is the right Cauchy–Green deformation tensor given as $[\mathbf{F}_{tot}(1)]^T \cdot \mathbf{F}_{tot}(1)$ with the total deformation gradient tensor $\mathbf{F}_{tot}(1) = \mathbf{F}_{vol} \cdot \mathbf{F}_{III}^{sem} \cdot \mathbf{F}_{II} \cdot \mathbf{F}_I(1)$ and its transpose $[\mathbf{F}_{tot}(1)]^T$. For the SFTSs for the variants 2 and 3, we simply apply the rotational symmetric operations around x_2 axis by 120° ($= 2\pi/3$) and 240° ($= 4\pi/3$), respectively, as demonstrated in Fig. 1(b):

$$\mathbf{E}_{ij}^{000}(2) = \mathbf{a}_{ik}^R(2) \cdot \mathbf{a}_{jl}^R(2) \cdot \mathbf{E}_{kl}^{000}(1), \quad (14)$$

$$\mathbf{E}_{ij}^{000}(3) = \mathbf{a}_{ik}^R(3) \cdot \mathbf{a}_{jl}^R(3) \cdot \mathbf{E}_{kl}^{000}(1), \quad (15)$$

where $[\mathbf{a}_{ik}^R(2)]$ and $[\mathbf{a}_{ik}^R(3)]$ are the corresponding rotational transformation matrices for variant 2 and 3, respectively. *Supplemental material S2* includes examples of computed SFTSs.

To account for the inhomogeneous elastic responses in polycrystalline α -Zr containing δ -hydrides, we adapted the eigenstrain and elasticity models developed in our prior work [52]. We formulate the position-dependent total eigenstrain tensor (\mathbf{E}_{ij}^0) as the

following:

$$\mathbf{E}_{ij}^0(\vec{r}) = \sum_g \theta(g, \vec{r}) \sum_p \mathbf{E}_{ij}^{00}(g, p, \vec{r}) \cdot H(\eta_{pg}), \quad (16)$$

where $\theta(g, \vec{r})$ is the grain shape function that identifies the g th grain ($\theta = 1$ within the grain and $\theta = 0$ outside), and $H(\eta_{pg})$ is the piecewise interpolation function of a structural order parameter η_{pg} ($H = \eta_{pg}$ for $\epsilon \leq \eta_{pg} \leq (1 - \epsilon)$ and $H = \eta_{pg}^3(6\eta_{pg}^2 - 15\eta_{pg} + 10)$ for $\eta_{pg}(\epsilon$ or $\eta_{pg})(1 - \epsilon)$ with a small value ϵ). Note that the high order polynomial near $\eta_{pg} = 0$ or 1 is employed to minimize the unphysical shift of η_{pg} approaching the equilibrium values ($\eta_{pg} = 0$ or 1), which can arise from the strain energy contribution. To define the SFTSs in individual grains, we apply the rotational axis transformation by $[\mathbf{a}_{ik}^G(g)]$ from the grain local $x_1 - x_2 - x_3$ coordinate system defined on the given g th grain to the global reference $X - Y - Z$ coordinate system. In addition, we employed a possible transformation strain relaxation factor near a grain boundary [53] by introducing the relaxation function $\varphi(\vec{r})$. This relaxation factor implicitly considers the structural variant-grain boundary interactions in our model. Therefore, the SFTS within the g th grain is given as

$$\mathbf{E}_{ij}^{00}(g, p, \vec{r}) = \varphi(\vec{r}) \cdot \mathbf{a}_{ik}^G(g) \cdot \mathbf{a}_{jl}^G(g) \cdot \mathbf{E}_{kl}^{000}(p), \quad (17)$$

where $\varphi(\vec{r}) = [\rho \cdot (\phi_{max} - \phi) + (\phi - \phi_{min})] / [\phi_{max} - \phi_{min}]$ with the relaxation parameter ρ ($\rho = 1$: no relaxation, $\rho = 0$: full relaxation), $\phi = \sum_g \psi_g^2$, and $\mathbf{E}_{kl}^{000}(p)$ is the SFTS in the reference grain, which is defined in Eqs. (13)–(15). For the position-dependent elastic modulus tensor (\mathbf{C}_{ijkl}), we use the following mathematical expression:

$$\mathbf{C}_{ijkl}(\vec{r}, T) = \sum_g \theta(g, \vec{r}) \cdot [h_g(\{\eta_{pg}\}) \cdot \mathbf{C}_{ijkl}^\delta(g, T) + (1 - h_g(\{\eta_{pg}\})) \cdot \mathbf{C}_{ijkl}^\alpha(g, T)], \quad (18)$$

where $\theta(g, \vec{r})$ is the grain shape function, $h(\{\eta_{pg}\})$ is the interpolation function that is consistently employed as in Eqs. (3) and (4) for smoothly connecting parameters for the two phases. The elastic moduli of the δ and α phases within the g th grain are also defined by applying the rotational axis transformation to the elastic moduli in a reference grain as the following:

$$\mathbf{C}_{ijkl}^\delta(g, T) = \mathbf{a}_{im}^G(g) \cdot \mathbf{a}_{jn}^G(g) \cdot \mathbf{a}_{ko}^G(g) \cdot \mathbf{a}_{lp}^G(g) \cdot \mathbf{C}_{mnop}^{\delta,ref}(T), \quad (19)$$

$$\mathbf{C}_{ijkl}^\alpha(g, T) = \mathbf{a}_{im}^G(g) \cdot \mathbf{a}_{jn}^G(g) \cdot \mathbf{a}_{ko}^G(g) \cdot \mathbf{a}_{lp}^G(g) \cdot \mathbf{C}_{mnop}^{\alpha,ref}(T), \quad (20)$$

where $\mathbf{C}_{mnop}^{\delta,ref}(T)$ and $\mathbf{C}_{mnop}^{\alpha,ref}(T)$ are the temperature-dependent elastic moduli of δ and α phases, respectively, defined in a reference grain with respect to the $x_1 - x_2 - x_3$ coordinate system (see Fig. 1(a)). These moduli in the $x_1 - x_2 - x_3$ coordinate system are obtained by applying the axis transformation to the moduli defined on their regular Cartesian coordinate system. Note that the elastic moduli of δ and α phases defined on the same $x_1 - x_2 - x_3$ coordinate system automatically satisfy the associated orientation relationship.

2.3. Governing kinetic equations

The structural order parameters (η_{pg}) and the hydrogen composition (u) interactively coevolve in a way to eliminate the thermodynamic driving force [21]. To simulate the temporal and spatial evolution of η_{pg} in a polycrystal, we employ the modified Allen-Cahn (or time-dependent Ginzburg–Landau) equation [53,77] written as the following:

$$\frac{\partial \eta_{pg}}{\partial t} = \theta(g, \vec{r}) \left[-L \left(\frac{\partial f}{\partial \eta_{pg}} + \omega_\eta \cdot \frac{\partial q}{\partial \eta_{pg}} - \kappa_{\eta,ij}^g \nabla_i \nabla_j \eta_{pg} + \frac{\partial e_{coh}}{\partial \eta_{pg}} \right) + \zeta_g(\vec{r}, t) \right], \quad (21)$$

where $\theta(g, \vec{r})$ is the grain shape function ($\theta = 1$ within the g th grain, $\theta = 0$ outside the g th grain), and L is the kinetic coefficient (note that we chose a large L ($L = 0.187 \times 10^2 m^3 / (J \cdot s)$) for guaranteeing a diffusion-controlled process), and $\zeta_g(\vec{r}, t)$ is the Gaussian Langevin noise term [53]. We chose $\omega_\eta = 1.0 \times 10^9 J/m^3$ for the structural transformations. The anisotropic gradient energy coefficient $\kappa_{\eta,ij}^g$ is taken into account in differently oriented grains using the transformation, $\kappa_{\eta,ij}^g = a_{ik}^G(g) \cdot a_{jl}^G(g) \cdot \kappa_{\eta,kl}^{ref}$. The numerical algorithm to solve Eq. (21) can be found in our prior work [53].

For the composition field u , we solve the Cahn–Hilliard equation [78] for polycrystalline materials as the following:

$$\frac{\partial u}{\partial t} = \nabla \cdot \left[h(\{\eta_{pg}\}) M_\delta \nabla \left(\frac{\partial f_m^\delta}{\partial u_\delta} \right) + (1 - h(\{\eta_{pg}\})) M_\alpha \nabla \left(\frac{\partial f_m^\alpha}{\partial u_\alpha} \right) \right] - \nabla \cdot M \nabla (m_g g(\{\psi_g\})) - \nabla \cdot M \nabla (\kappa_u \nabla^2 u) + \zeta_c(\vec{r}, t), \quad (22)$$

where M_δ and M_α are the atomic diffusion mobilities of H in δ - and α -phases, respectively, and $\zeta_c(\vec{r}, t)$ is the Gaussian Langevin noise term. These mobilities are parameterized by the self-diffusivity in our study using the Einstein relation: $M_\phi = D_\phi^{self} / (F_\phi RT)$, where D_ϕ^{self} is the self-diffusivity, F_ϕ is the tracer correlation factor determined by the crystallographic structure for phase ϕ ($=\alpha, \delta$) ($F_\alpha = 1$ for the interstitial diffusion of hydrogen in a dilute solid solution, and $F_\alpha = 0.740$ for interstitial diffusion of hydrogen in a concentrated solid solution ZrH_{1.58} [79]), R is the gas constant, and T is the temperature. The phase-dependent diffusion mobility is modeled as $M = h(\{\eta_{pg}\}) \cdot M_\delta + (1 - h(\{\eta_{pg}\})) \cdot M_\alpha$. In addition, the equal chemical potential condition ($\partial f / \partial u = \partial f_m^\delta(u_\delta) / \partial u_\delta = \partial f_m^\alpha(u_\alpha) / \partial u_\alpha$) is applied to derive the first term of Eq. (22). To numerically solve Eq. (22), we employed the semi-implicit Fourier-spectral method [80,81].

Note that the field variables are naturally coupled through the variational derivatives of the free energy functional defined in Eq. (1). However, since both elastic modulus and eigenstrain are functions of only the structural order parameter, the strain contribution is only shown in Eq. (21). For computing the internal strain energy generated by the hydride formation for solving Eq. (21), we use the mathematical formalism from the Khachaturyan microelasticity theory [71]. Assuming that the mechanical equilibrium is established much faster than the diffusional and displacive (or structural) transformations, we solve the following mechanical equilibrium equation based on the linear elasticity theory:

$$\nabla_j \cdot \sigma_{ij} = \nabla_j \cdot [C_{ijkl}(\vec{r}) \varepsilon_{kl}^{el}(\vec{r})] = 0. \quad (23)$$

In Eq. (23), the elastic strain (ε_{ij}^{el}) is written as $\varepsilon_{ij}^{el}(\vec{r}) = \tilde{\varepsilon}_{ij} + \delta \varepsilon_{ij}(\vec{r}) - E_{ij}^0(\vec{r})$, where $\tilde{\varepsilon}_{ij}$ is the homogeneous strain that represents the macroscopic volume change, $\delta \varepsilon_{ij}$ is the heterogeneous strain that represents the local strain perturbation, and E_{ij}^0 is the eigenstrain. Note that we consider the eigenstrain with mixed coherency and inhomogeneous elastic modulus described in Eqs. (16) and (18), respectively. We numerically solve Eq. (23) using the Fourier-spectral iterative perturbation method [82,83]. We then compute the coherency strain energy by $(1/2) \cdot C_{ijkl}(\vec{r}) \cdot \varepsilon_{ij}^{el}(\vec{r}) \cdot \varepsilon_{kl}^{el}(\vec{r})$ assuming the linear elasticity.

3. Computer simulation results and discussions

This section presents our phase-field simulations and corresponding analyses. We purposely chose the time and length scales with $\Delta x = \Delta y = \Delta z = 0.4 \text{ nm}$ and $\Delta t = 5.3590 \times 10^{-13} \text{ s}$ to resolve the microscopic microstructural mechanisms at early stages of hydride formation. Note that the time and length scales within this model can be extended employing coarser grid spacing and

longer time intervals if one simulates the later stages of coarsened hydride microstructures. These extended scales will require hypothetically thicker metal/hydride interfaces, for which the equal chemical potential condition implemented in our model eliminates the unphysical interfacial potential [67] as we discussed above. However, the interfacial coherency needs to be appropriately modified to consider the coarsened hydrides that inevitably generate enormous strain energy if the interface is assumed to be coherent. Therefore, significant coherency loss is expected. In addition, some microscopic characteristics (e.g., multivariant micro-platelets) may not be resolved by the coarser grid spacing, which will require a new definition of the structural order parameter that can implicitly include the microscopic aspects (e.g., order parameter that defines a macro-platelet).

We numerically solve the governing equations in the nondimensionalized forms by $\Delta x^* = \Delta x / l_0$, $\Delta t^* = \Delta t / t_0$, $f^* = f / E_0$, $\omega_\eta^* = \omega_\eta / E_0$, $m_g^* = m_g / E_0$, $\kappa^* = \kappa / (E_0 \cdot l_0^2)$, $C_{ij}^* = C_{ij} / E_0$, $L^* = L \cdot t_0 \cdot E_0$, $D^* = D / D_0$ and $\nabla^* = l_0 \cdot \nabla$, where l_0 ($= 1.0 \times 10^{-9} \text{ m}$) is the characteristic length, E_0 ($= 1.0 \times 10^9 \text{ J/m}^3$) is the characteristic energy, D_0 ($= 1.866 \times 10^{-8} \text{ m}^2/\text{s}$) is the characteristic diffusivity, and t_0 ($= l_0^2 / D_0 = 5.3590 \times 10^{-11} \text{ s}$) is the characteristic time. We include the corresponding input parameters including the CALPHAD database for the Zr-H system in *Supplemental material S4*, and temperature-dependent elastic moduli, temperature-dependent lattice parameters, and hydrogen diffusivities in *Supplemental material S5*. To verify the thermodynamically-consistent implementation of the thermodynamic model with the database and the interfacial parameters within our modeling framework, we first analyzed the simulated fundamental thermodynamic equilibrium and interfacial properties in *Supplemental material S3*.

3.1. Morphological instability of multivariant hydride microstructures

The hydride precipitate morphology is generally determined by the coupled anisotropies in interfacial energy and coherency strain energy. Assuming that the strain energy is a more dominant factor than the interfacial energy for hydride formation involving large volume expansion, we first consider the strain energy anisotropy that may dictate hydride morphology. One of the key variables in our SFTS model in Eq. (13) for hydride formation is the interfacial coherency state within the mixed coherency concept. In particular, the lattice mismatch ν_{sem} in Eq. (11) of our model can be modified to represent the variation of the interfacial coherency state between hydride and matrix phases. To investigate the impact of the coherency state, we first explore the morphological change of the hydride with the varying lattice mismatch.

To determine the strain energy-driven orientation of the habit plane (i.e., phase boundary) between the hydride and matrix phases, we numerically identify the interface normal $\vec{n}_0 = (n_1^0, n_2^0, n_3^0)$ that minimizes the orientation-dependent coherency strain energy density $B(\vec{n}) = C_{ijkl} E_{ij}^{000}(1) E_{kl}^{000}(1) - n_i \sigma_{ij}^0 \Omega_{jk} \sigma_{kl}^0 n_l$, where $\sigma_{ij}^0 = C_{ijkl} E_{kl}^{000}(1)$, and $\Omega_{jk}^{-1} = C_{jilk} n_i n_l$, as a function of the misfit parameter q following the Khachaturyan microelasticity theory [71,76]. Since this theory is based on the homogeneous elastic modulus approximation, we use the average modulus of δ -hydride and matrix (α -Zr) phase. Specifically, we note that we trace n_2^0 ($= \cos(\psi)$, see the inset of Fig. 2(a)), which indicates the angle between the x_2 axis and \vec{n}_0 , to characterize the experimentally relevant morphological re-orientation tendency with respect to the x_2 axis later. The habit plane with $n_2^0 = 1$ is aligned normal to x_2 (i.e., parallel to the basal plane), while one with $n_2^0 = 0$ is aligned along x_2 (i.e., parallel to the prismatic plane). Fig. 2(a) shows the computed variation of n_2^0 as a function of the misfit parameter q . Interestingly, two distinct habit plane modes are identified for this system as shown in Fig. 2. One (Mode II) of the two habit plane

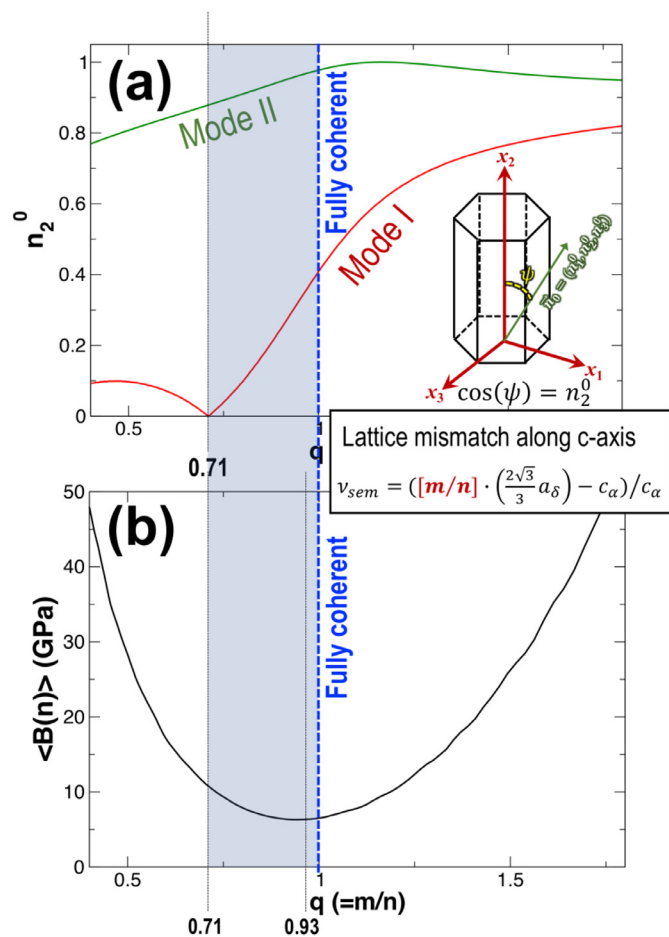


Fig. 2. (a) Variation of $n_2^0 (= \cos(\psi))$ as a function of the misfit parameter q ; and (b) Average strain energy density ($\langle B(\vec{n}) \rangle$) over all possible phase boundary orientations for the given misfit parameter q .

modes is more aligned with the basal plane in the *hcp* coordinate system in Fig. 1, and its orientational variation with changing p is relatively flat. On the other hand, the orientation of the other habit plane mode (Mode I) changes more drastically with varying q , and the variation becomes more sensitive to the misfit parameter q when n_2^0 approaches 0, which corresponds to the boundary parallel to the prismatic plane. We also trace the variation of the overall strain energy for different coherent states. To characterize the overall strain energy, we computed the average strain energy density ($\langle B(\vec{n}) \rangle$) over all possible phase boundary orientations for the given misfit parameter q assuming that all possible phase boundary orientations can be expressed. Fig. 2(b) shows the computed $\langle B(\vec{n}) \rangle$ as a function of the misfit parameter q . Note that this quantity alone does not determine the specific coherency state accommodating the given volume expansion. Rather, the $\langle B(\vec{n}) \rangle$ profile in Fig. 2(b) might carry the information about the energetic propensity of the phase boundary orientation with the varying coherency state. Intriguingly, the strain energy profile bears a minimum at a certain coherency state ($q = 0.93$). This is mainly because our SFTS model incorporates the conservation of the volumetric strain upon the variation of the coherency state. Note that the characteristic strain energy landscape becomes flatter when the misfit strain parameter q approaches a minimum. This may indicate that the coherency state can relatively easily vary near this minimum from the strain energy penalty point of view since it does not require significant variation in the strain energy upon changing the coherency state (*i.e.*, misfit parameter q).

It should be emphasized that the above theoretical analysis only applies to the single variant case. Although the analyzed morphological tendency is an important basis for explaining the physical factors determining the multivariant hydride microstructure, elastic interactions among different variants cannot be fully described by the analysis. Moreover, this analysis does not carry the impact of the interfacial energy anisotropy although it could be less impactful compared to the strain energy when a large volume change is involved. To directly investigate the hydride morphological behaviors when the multiple variants and interfacial energy anisotropy are simultaneously involved, we designed and performed 3D ($288\Delta x \times 288\Delta y \times 288\Delta z$) control phase-field simulations employing a finite number of hydride particles with different structural variants are equally assigned, in the supersaturated α -Zr matrix (with overall composition $u_0 = 0.2$) as shown in Fig. 3(a). To promote the kinetic interactions between different variants during their growth, we purposely populated those particles in a way that those hydride particles are closely located to each other. Fig. 3 (b–g) shows the cross sections of the simulation results at $t = 20,000\Delta t$ for different magnitudes of the misfit parameter q .

First of all, our simulations clearly indicate that the multivariant hydride morphology is highly sensitive to the misfit parameter q . As q increases up to the fully coherent state ($q=1$), the multivariant hydride microstructure becomes morphologically more unstable. More specifically, for $q = 0.72 \sim 0.84$, δ -hydride variants exhibit stacking behaviors, while the individual variants tend to independently grow for $q = 0.92 \sim 1.00$. In the case of $q = 0.88$, both behaviors are observed at the same time. Importantly, these microstructural behaviors can be understood by considering the coupled anisotropic effects of coherency strain energy and interfacial energy. Note that the phase boundary orientation analysis based on the coherency strain energy density $B(\vec{n})$ and interfacial energy anisotropies determines the equilibrium shape of a precipitate in principle. On the other hand, this analysis may provide the information about the kinetic morphological tendency in terms of orientation for the growing precipitate before reaching the equilibrium state as illustrated in Fig. 4(a). To specifically observe the impacts of these anisotropies, we compare the early stages of the temporal evolution of hydride variants for the cases with $q = 0.80$ (mixed coherency) and $q = 1.00$ (full coherency) as shown in Fig. 4(b).

As one can see from the figure, for $q=1.00$, individual hydride variants tend to grow in a direction almost parallel to the basal plane since one (Mode II) of habit plane modes in Fig. 2(a) is quite close to the basal plane (*i.e.*, $n_2^0 = 1$) and the other mode (Mode I) highly deviates from $n_2^0 = 0$. In this case, the growth tendency along the basal plane can be synergistic with the anisotropy in the interfacial energy, which is smaller along the basal plane direction as discussed above (also see the illustration in Fig. 4(a)). Therefore, individual variants have a strong growth tendency along the basal plane direction. Note that this behavior lowers the chance that the growing variants meet to form twin boundaries. Therefore, the stacking behavior is rarely observed. On the other hand, for the case with $q = 0.80$, the growth direction of individual hydride variants is more inclined toward the direction along the x_2 -axis as shown in Fig. 4(b). This behavior may be governed by the combined effects of the identified habit plane modes (or growth tendencies) in Fig. 2(a). The interface normal of Mode I is almost perpendicular to the x_2 axis (n_2^0 is close to 0) and n_2^0 of Mode II is smaller than the fully coherent ($q=1.00$) interface counterpart. As a result, the growing variants are more likely to meet together to form twin boundaries parallel to the basal plane. Note that the corresponding twin boundary energy is 0.080 J/m^2 in our model according to our numerical calculations using the formula

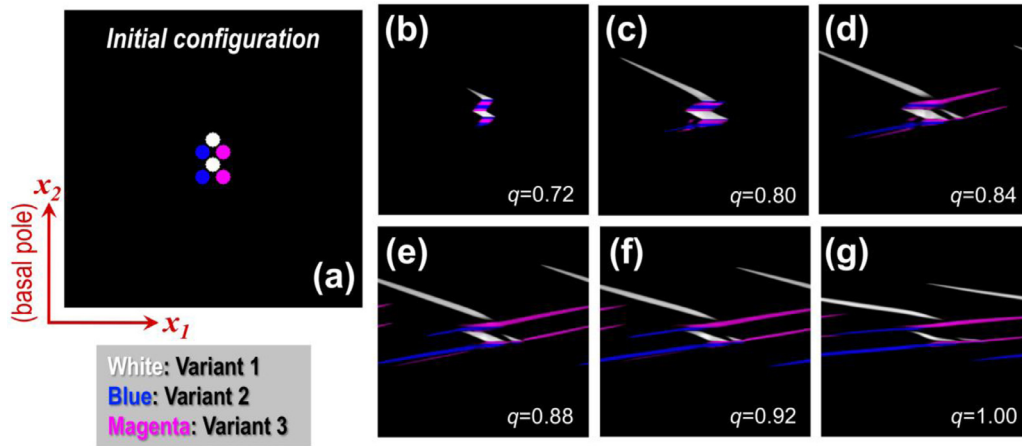


Fig. 3. Cross sections of 3D ($288\Delta x \times 288\Delta y \times 288\Delta z$) control phase-field simulations: (a) Embedded 6 δ -hydride particles in α -Zr as an initial configuration; (b–g) Multi-variant hydride microstructures for several misfit parameter q at 20,000 Δt .

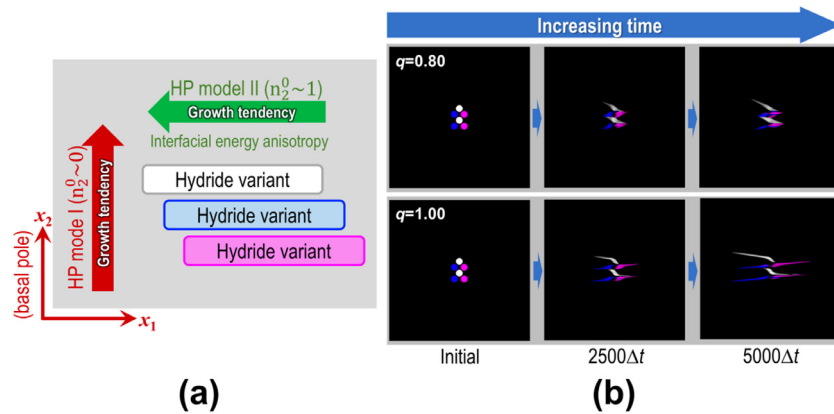


Fig. 4. (a) Illustration of growth tendencies associated with the two habit plane (HP) modes; and (b) Initial stage of multivariant microstructure evolution for two selected coherency states (white: variant 1, blue: variant 2, magenta: variant 3). (For interpretation of the references to color in this figure legend, the reader is referred to the web version of this article.)

in Eq. (S4). This is even smaller than the interphase boundary energy along the basal plane between α - and δ -phases. In addition, by forming twin boundaries (*i.e.*, by stacking variants), the shear strain components of the transformation strain can be cancelled out (*i.e.*, strain accommodation). For example, this can be noticed by summing shear strain tensor components of our SFTSs in Table S1 over all three variants (*i.e.*, $\sum_{p=1}^3 E_{ij}^{000}(p)$ for $i \neq j$), resulting in zero. This indicates that those twin boundaries are energetically stable and can be maintained even at later stages once they are formed, which explains the formation of a morphologically more stable macro-platelet (or a variants packet) consisting of several hydride micro-platelets for $q = 0.72 \sim 0.84$. Note that the growth direction of the macro-platelet is effectively inclined toward a direction normal to the basal plane by alternating the variants. This stabilized stacking behavior may explain a coarse stacking structure of multiple hydride plates at later stages of hydriding as experimentally observed (see Fig. S3 in Supplemental material S6 for the transmission electron microscopy (TEM) images).

3.2. Hydride formation and possible reorientation mechanisms

In the previous section, we focused on specifically controlled hydride microstructural configurations. In this section, we investigate more naturally formed hydride microstructures. For this purpose, we designed relaxed 3D ($288\Delta x \times 288\Delta y \times 288\Delta z$) phase-field simulations incorporating random fluctuations of or-

der parameters and composition fields to capture more realistic hydride microstructures precipitated in supersaturated Zr–H solid solutions (with the overall composition $u_0 = 0.17$). This simulation setup can be considered as the undercooled solid solution after a dissolution process [31,62–64]. To focus on the interactions among the hydride variants, we did not include grain boundaries in these simulations. We performed simulations for different coherent states ranging from $q = 0.72$ to $q = 1.00$. We found that, for $q < 0.80$, the simulation system is stuck in metastable states where the entire simulation domain is occupied by wide hydride layers without forming α/δ interfaces (*i.e.* multilayer system). The order parameter values significantly deviate from their equilibrium values. This can be somehow explained by the strain energy argument. According to our calculations in Fig. 2(b), the average strain energy $\langle B(\vec{n}) \rangle$, which is associated with the coherency strain energy density arising from the α/δ interphase boundary, becomes large as the misfit parameter q decreases. We speculate that the strain energy penalty for forming the interphase boundaries for $q < 0.80$ is too large for the system to accommodate. Therefore, the system is rather likely to only form twin boundaries that can reduce the total strain energy and interfacial energy within the system. Since we are not sure if this state is real, we exclude these cases from our analyses and discussion.

Fig. 5 shows the simulated hydride microstructures for selected cases of q , which clearly exhibit separated hydride precipitates from the parent phase. For the fully coherent case ($q = 1.00$)

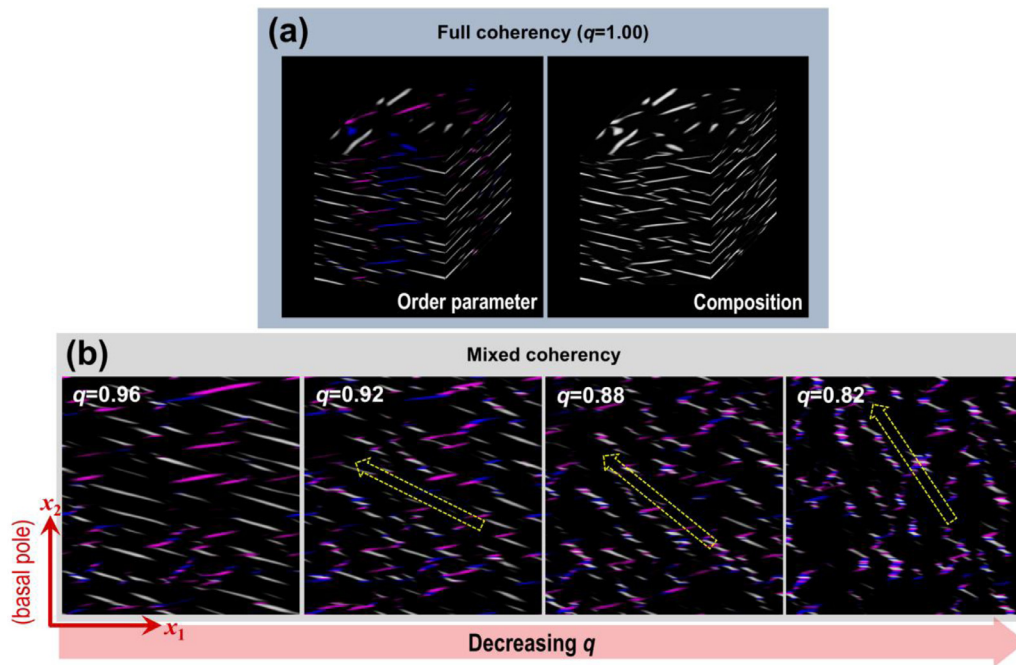


Fig. 5. Simulated 3D hydrides microstructures (white: variant 1, blue: variant 2, magenta: variant 3 for order parameters) in Zr single crystals at $t = 50,000\Delta t$ formed by random fluctuations of order parameters and composition for (a) fully coherent interfaces (left: 3D order parameter profile, right: 3D composition profile); and (b) mixed coherent interfaces with decreasing q (cross sections of order parameter profiles). (For interpretation of the references to color in this figure legend, the reader is referred to the web version of this article.)

in Fig. 5(a), the individual variants grow mostly independently without forming twin boundaries. However, as q decreases for the mixed coherency case in Fig. 5(b), more stacking behaviors to form macro-platelets are clearly observed (see the cases with $q = 0.82, 0.88$). This trend is consistent with the results of our control simulations in Section 3.1 (see Fig. 3). In addition, the formation of a macro-platelet consisting of several micro-platelets of Zr hydrides were discussed by Chung et al. [84]. Note that the effective growth direction of the macro-platelet is also affected by the misfit parameter q . In particular, the case with $q = 0.82$ includes the macro-platelets more aligned along x_2 axis than the case with $q = 0.88$ or $q = 0.92$. More importantly, this behavior is directly connected to the hydride re-orientation under the applied load. Experimental observations clearly demonstrate the re-oriented hydride microstructures as a result of dissolution and re-precipitation during heating and cooling cycles under load [31,62–64]. Our simulation results and theoretical analysis may capture and explain the experimentally observed hydride re-orientation behaviors. As explained in our simulations, the stacking behaviors and the effective growth direction of the macro-platelets are sensitive to the misfit parameter q (i.e., coherency state along the c -axis (or x_2 -axis)). In addition, as discussed above, the phase boundary alignment driven by Mode I in Fig. 2(a) is highly sensitive to q within the range of $0.71 < q < 1.00$. At the same time, the average strain energy density $\langle B(\vec{n}) \rangle$ is flat near its minimum ($q = 0.93$). All these analyses may explain the propensity of introducing structural defects for varying the coherency state to accommodate the large volume expansion under applied load. This is because varying the misfit parameter q near 0.93 does not require a large strain energy penalty in spite of the drastic change in the growth tendency of the hydride variant. We speculate that this is also evidenced by the characteristic diffraction signature indicating permanent peak broadening from the synchrotron x-ray diffraction experiments for the reprecipitated/re-oriented hydrides [31,62]. The possibility of the peak broadening caused by strain broadening due to elastic and/or plastic strains arising from structural defects

(e.g., dislocations) is also discussed in the experimental study [62]. Considering all these factors, we propose a possible re-orientation mechanism that the applied load induces structural defects that destroy the coherency of hydride/metal interfaces along the c -axis and result in the stacking behaviors of hydride micro-platelets, resulting in a macro-platelet effectively aligned along the c -axis.

3.3. Elastic interactions between applied stress and hydrides

The mechanism proposed in the previous section is associated with the inelastic interactions between the applied load and hydride variants. In this section, we explore the elastic interactions that may affect the hydride microstructures. We considered several types of applied stresses to account for possible applied loading conditions in service of cladding Zr alloys. We also performed 3D ($288\Delta x \times 288\Delta y \times 288\Delta z$) phase-field simulations incorporating random fluctuations of η_{pg} and u fields under the applied stress conditions. For the interfacial coherency state, we first chose the fully coherent case ($q = 1.00$) to isolate the effect of the applied stress. Fig. 6(a) and (b) shows simulated 3D hydride microstructures under an applied normal stress along the x_1 direction ($\sigma_{11}^{appl} = 500\text{MPa}$) and an applied shear stress ($\sigma_{12}^{appl} = -50\text{MPa}$), respectively, as examples. For both loading conditions, we could observe that only two hydride variants (variants 2 and 3) are selected to nucleate and grow. The hydride microstructural behavior under the applied shear stress can be understood by the fact that the SFTSs for those two variants contain the negative shear components, which are aligned with the applied shear stress direction, in contrast to variant 1 as shown in Table S1. As a result, individual variants may differently respond to the shear stress. However, variant selection under an applied normal stress cannot be explained by the argument associated with the SFTSs since all three variants have the same normal components of the SFTS along the x_1 direction. Rather, we speculate that the anisotropic elastic moduli of the differently oriented variants may respond differently to the uniaxial stress along the x_1 direction.

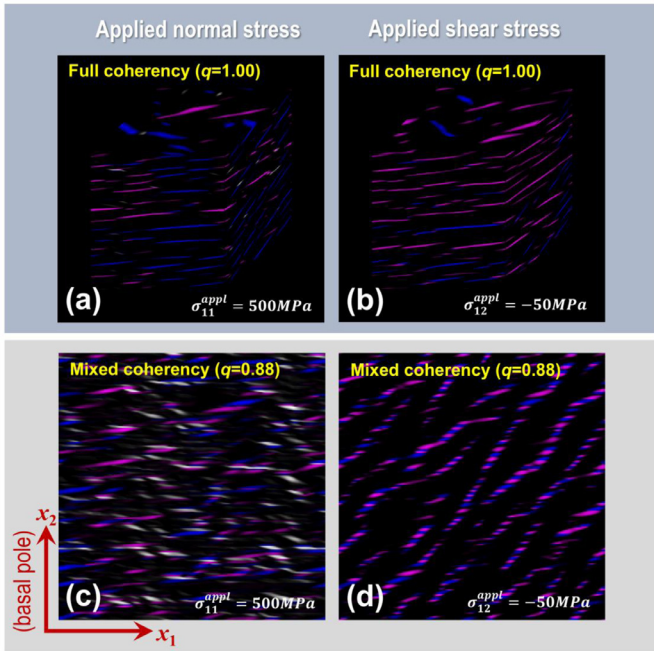


Fig. 6. Simulated Zr hydrides microstructures (at $t = 50,000\Delta t$) under applied loads (white: variant 1, blue: variant 2, magenta: variant 3): (a) Fully coherent case under the applied normal stress ($\sigma_{11}^{appl} = 500\text{MPa}$); (b) Fully coherent case under the applied shear stress ($\sigma_{12}^{appl} = -50\text{MPa}$); (c) Mixed coherent case under the applied normal stress ($\sigma_{11}^{appl} = 500\text{MPa}$); and (d) Mixed coherent case under the applied shear stress ($\sigma_{12}^{appl} = -50\text{MPa}$). (For interpretation of the references to color in this figure legend, the reader is referred to the web version of this article.)

Motivated by the identified variant selection behavior under the applied stress for the fully coherent case, we next explore the coupled effects of coherency loss and applied stress. We choose the misfit parameter $q = 0.88$, for which the hydride variants exhibit both stacking and independent growth behaviors under no applied stress as discussed in Section 3.1. We also performed 3D phase-field simulations for the mixed coherent case under the same applied stress conditions as the fully coherent cases discussed above. Fig. 6(c) and (d) shows the x_1 - x_2 cross sections of the simulated hydride microstructures under the applied normal stress ($\sigma_{11}^{appl} = 500\text{MPa}$) and the applied shear stress ($\sigma_{12}^{appl} = -50\text{MPa}$), respectively. To better capture the impact of the applied stress, these microstructures can be compared with ones with the same coherency state ($q = 0.88$) without the applied stress in Fig. 5(b). For the applied normal stress, the variant selection does not effectively occur in contrast to the fully coherent case. Therefore, we may conclude that the pure elastic interactions between the normal stress and hydrides cannot explain the variation of the hydride microstructural features when mixed coherency is involved.

On the other hand, under an applied shear stress, only variants 2 and 3 are expressed as we observe in the fully coherent case. More importantly, the stacking tendency consisting of those two variants is enhanced compared to the case without an applied shear stress. As a result, the clearly defined macro-platelets including the two variants are more aligned with the x_2 -axis (or c -axis). Therefore, this coupled effect can be another type of the re-orientation mechanism for hydride formation under applied load. As we mentioned, hydride re-orientation phenomenon is observed when precipitation occurs under an applied tensile stress higher than a threshold value [31,62–64]. However, we note that, under an applied normal stress, some grains of a polycrystalline Zr alloy specimen can be locally under an applied shear stress depending on the sample geometry and/or the grain orientation especially

for the elastically anisotropic materials. In addition, according to our simulation, the variant selection behavior can occur even under a small magnitude ($\sim 50\text{MPa}$) of shear stress. Hence, if the coherency loss can be established by the applied stress, the proposed re-orientation mechanism mediated by those coupled effects may readily operate in polycrystalline Zr alloys.

3.4. Effects of grain boundaries in polycrystals

So far, we have considered hydride formation in a single crystal. However, Zr alloys in service contain multiple grains separated by grain boundaries (GBs). Therefore, GB-hydrogen and/or GB-structural variant interactions can play key roles in determining selective hydride nucleation behaviors at GBs [85,86] and associated hydride microstructures. However, our understanding of roles of GBs has yet to be established. In this section, we interrogate the impacts of grain boundaries on hydride microstructure formation. For simulating the formation of hydrides interacting with GBs, we employed 3D ($288\Delta x \times 288\Delta y \times 288\Delta z$) static grain structures, which were generated by the phase-field grain growth model [87,88] of which details can be found in our previous work [53].

To isolate the effects of GBs, we first consider a simple bi-crystal that contains a flat GB, which accounts for all the modeling factors associated with the interactions with a GB. To exclude the effects of grain-to-grain misorientation, we assigned 0° to one grain and 180° to the other grain. We generated two representative types of bi-crystals: one containing a GB parallel to the basal plane (*i.e.*, parallel to x_1 - x_3 plane, GB type 1, see Fig. 7(a)); and the other containing a GB perpendicular to the basal plane (*i.e.*, parallel to x_2 - x_3 plane, GB type 2, see Fig. 7(b)). Note that GBs are also formed at top and bottom planes in Fig. 7(a), and left-hand side and right-hand side planes in Fig. 7(b) in our simulation domains due to the applied periodic boundary condition. First of all, we investigate the effects of the hydrogen-GB interaction strength by varying the magnitude of the interaction parameter m_g in the free energy functional in Eq. (1) for the two cases of bi-crystals. Note that the interaction parameter m_g is related to the grain boundary segregation potential, which is determined by the grain boundary energy variation with segregating hydrogen at a grain boundary. We choose the mixed coherency case with $q = 0.82$ for those cases. We set the GB relaxation parameter (ρ of $\varphi(\vec{r})$ in Eq. (17)) to be 1.0 to exclude the effects of the relaxation of the transformation strain at a GB.

Fig. 7(c–e) shows the hydride variants microstructures with GB type 1 and Fig. 7(f–h) shows the microstructures with GB type 2 for increasing m_g . In both cases, as the interaction becomes stronger, we noticed more hydrides formed at GBs. This is also evidenced by the expressed hydride densities at the top plane for GB type 1 and the right-hand side plane for GB type 2. This behavior should arise from the more grain boundary segregation of H [89] with the increasing interaction parameter m_g [61]. For the same bi-crystals, we also performed 3D simulations for different magnitudes of the GB relaxation parameter (ρ of $\varphi(\vec{r})$ in Eq. (17)) for the eigenstrain. In this case, we also employed non-tilted bi-crystals containing both GB types without grain boundary segregation of hydrogen ($m_g^* = 0.0$) to focus on the sole impact of the GB relaxation. Fig. 8 shows the simulated hydrides microstructures only for GB type 2 as an example. We varied the relaxation parameter from $\rho = 1.0$ (No relaxation) to $\rho = 0.5$ (half relaxation). As shown in the figure, the grain boundary relaxation effectively induces the grain boundary nucleated hydrides (see the hydride density on the right-hand side GB plane) by relaxing the energy barrier caused by the transformation strain, which is consistent with our prior work [53]. This is also true for the GB type 1 although these are not shown in the figure. This GB nucleation behavior seems qualitatively similar to that induced by the GB-solute

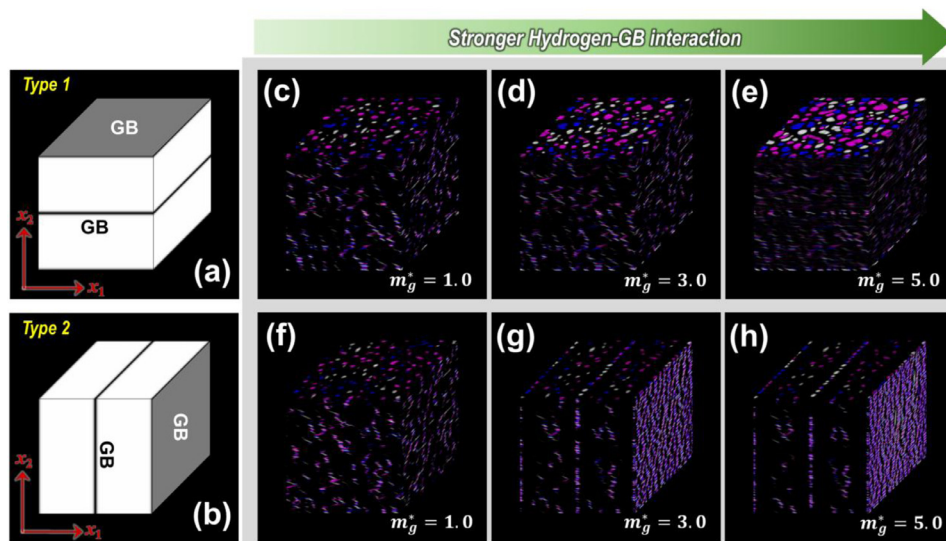


Fig. 7. Simulated δ -hydrides (with mixed coherency $q = 0.82$) microstructures (at $t = 40,000\Delta t$) in two representative bi-crystals of α -Zr (white: variant 1, blue: variant 2, magenta: variant 3). (a) Bi-crystal containing GB type 1; (b) Bi-crystal containing GB type 2; (c–e) δ -hydrides with GB type 1 with increasing m_g^* ; and (f–h) δ -hydrides with GB type 2 with increasing m_g^* . (For interpretation of the references to color in this figure legend, the reader is referred to the web version of this article.)

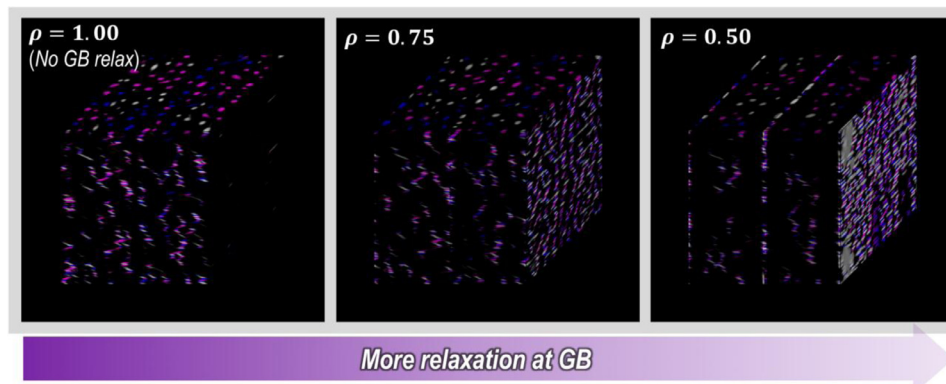


Fig. 8. Simulated δ -hydride (with mixed coherency $q = 0.82$) microstructures (at $t = 40,000\Delta t$) in α -Zr bi-crystals (GB type 2) with the decreasing GB relaxation parameter ρ (white: variant 1, blue: variant 2, magenta: variant 3). (For interpretation of the references to color in this figure legend, the reader is referred to the web version of this article.)

interaction discussed above. However, we note that the physical origin of GB nucleation is quite different. GB-solute interaction-induced nucleation is promoted by the GB segregation of hydrogen, which preferentially populate hydrogen at GB and results in the composition exceeding the solubility limit. On the other hand, GB relaxation-induced nucleation is driven by the lowered barrier for the structural transformation due to strain relaxation.

Importantly, as one can see from the figure, the hydride variants respond differently to the same GB-solute interaction parameter depending on types of GBs in terms of population density and morphology. Similar behaviors were also observed for the GB relaxation parameter. This different response cannot be solely explained by either GB segregation-induced or GB relaxation-induced nucleation. Rather, it can be rationalized by the geometric relationship between GB plane orientation and hydride growth direction since the multivariant hydride morphology and their growth behaviors are strongly anisotropic as we witnessed in our simulations in previous sections.

Fig. 9(c–f) shows the cross sections of simulated 3D hydride microstructures for $q = 0.82$ (mixed coherency) and $m_g^* = 3.0$ for the two types of GBs. For GB type 1, no significant effect of GB on the hydride variants morphology was observed (see Fig. 9(c) and (d) for the order parameter profile and the composition profile,

respectively). The hydride variants and hydrogen composition are slightly more populated at a GB (see the highlighted region by a yellow rectangle in Fig. 9(c) and (d)) than grain interior. On the other hand, for GB type 2, grain boundary hydrides exhibit significantly different morphological features compared to intragranular hydrides (see Fig. 9(e) and (f) for the order parameter profile and the composition profile, respectively). The grain boundary hydrides show the more compact stacking behavior and well aligned along the grain boundary plane (see the highlighted region by yellow rectangles in Fig. 9(e) and (f)). These observed behaviors in both cases indicate that the hydride variant-GB interaction can be synergistic when the effective growth direction of the hydride macro-platelet is aligned with the grain boundary plane orientation [89]. As discussed in Section 3.2, the macro-platelets of hydrides grow effectively along the c -axis (or x_2 -axis) for a misfit parameter $q = 0.82$, which is parallel to GB type 2. By the coupled effects of the GB segregation of hydrogen and the geometrical alignment, the micro-platelets tend to be localized at the GB, resulting in their stacking to form a macro-platelet growing along the grain boundary plane. This argument may be supported by the simulations for hydrides with the full interfacial coherency ($q = 1.00$). We carried out 3D phase-field simulations for this fully coherent case incorporating the two types of GBs. For GB type 1, in

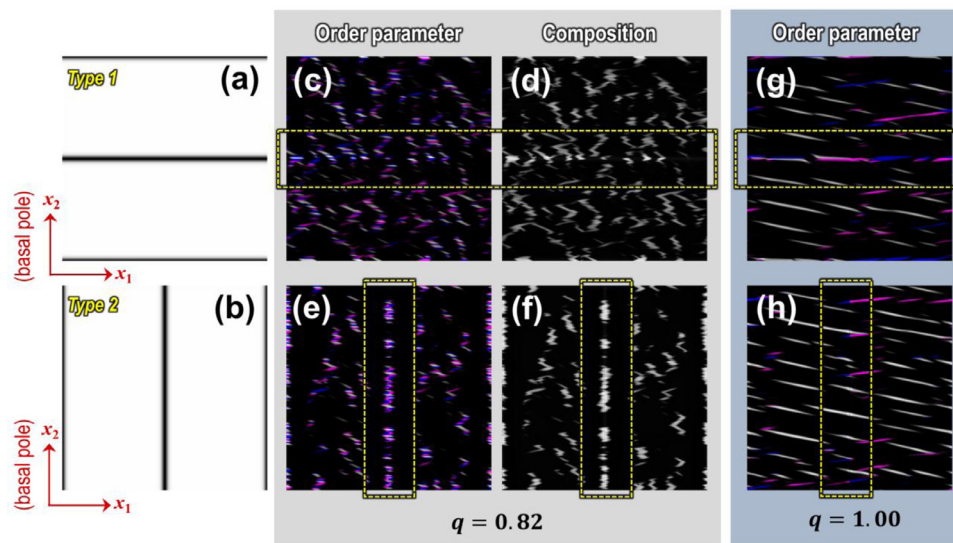


Fig. 9. Cross sections of simulated δ -hydrides microstructures (at $t = 40,000\Delta t$) in two representative bi-crystals (a,b) (with the GB-solute interaction parameter $m_g^* = 3.0$) of α -Zr. (c,d) Hydride microstructure for GB type 1 and $q = 0.82$; (e,f) Hydride microstructure for GB type 2 and $q = 0.82$; (g) Hydride microstructure for GB type 1 and $q = 1.00$; and (h) Hydride microstructure for GB type 2 and $q = 1.00$. White/blue/magenta represent variant 1/variant 2/variant 3. (For interpretation of the references to color in this figure legend, the reader is referred to the web version of this article.)

contrast to the mixed coherency case with $q = 0.82$, GB hydrides are localized at and aligned with the grain boundary plane as shown in Fig. 9(g) for the full interfacial coherency. On the other hand, as shown in Fig. 9(h) for GB type 2, the hydrides with the full interfacial coherency ($q = 1.00$) are not populated at the GB. As our simulations in the previous section demonstrated (see Fig. 5(a)), the individual hydride variants for the full coherency case grow in a direction more aligned along the basal plane without stacking behaviors. Therefore, those hydride variants can more easily interact with and reside at the geometrically more aligned GB type 1 than GB type 2 which is almost perpendicular to the variant growth direction. Recently, similar selective formation behaviors of intergranular hydrides in Zr alloys have been experimentally observed and analyzed by electron backscatter diffraction (EBSD) [90].

More importantly, these behaviors indicate an additional probable mechanism for hydride re-orientation associated with interactions with GBs. As proposed in Section 3.2, the applied load may tend to create structural defects, resulting in interfacial coherency loss. In this case, the hydride variants may interact more strongly and selectively with the grain boundaries perpendicular to the basal plane than other grain boundary orientations. However, when no structural interfacial defects are generated (due to small or no applied load), the variants are more selectively interact with the grain boundaries parallel to the basal plane. These *switching-like* behaviors of GB-hydride interactions responding to the interfacial coherency loss may enhance the re-orientation of hydrides caused by the applied load. We note that this mechanism may not be effective if the grain boundaries are mostly oriented in the circumferential direction (*i.e.*, GB type 1 are mostly expressed in a grain structure).

We next explore the impacts of the grain misorientation on the hydride microstructures. To account for the textured grains, we consider a slightly tilted bi-crystal for which only the right-hand side grain was rotated. We also choose the misfit parameter $q = 0.82$ (mixed coherency) and the GB-solute interaction parameter $m_g^* = 3.0$ for this case. Fig. 10 shows the cross sections of simulated 3D ($288\Delta x \times 288\Delta y \times 288\Delta z$) hydride microstructures. Notably, in the rotated right-hand side grain, only two variants are selected to nucleate and grow, exhibiting the stacking behavior.

This behavior is somewhat similar to the hydride microstructure under the shear stress as discussed in Section 3.3 (see Fig. 6(d)). The rotated right-hand side grain is mechanically constrained by a neighboring grain (left-hand side grain). At the same time, the neighboring grain contains hydrides that give rise to significant volume expansion. Therefore, it is possible that the volumetrically strained left-hand side grain may naturally exert the shear stress or strain on the right-hand side grain, resulting in variant selection.

We finally conducted 3D ($288\Delta x \times 288\Delta y \times 288\Delta z$) phase-field simulations of hydride formation in a polycrystal for demonstrating the simulation capability of the developed model. For the initial α -Zr microstructure, we prepared a static grain structure containing 13 grains (see Fig. 11(a)). The grain morphology in our grain structure is equiaxed so as to represent a generic grain microstructure. Note that the average grain size of the grain structure in our computational domain is much smaller than that of realistic polycrystalline Zr alloys. However, we also note that the generated grain structure is sufficient for running demonstrative simulations since it incorporates key physical factors discussed above. Polycrystalline Zr alloys in service exhibit a basal pole texture with the strong $\{0002\}$ pole intensity along the normal or radial directions [31]. For simplicity, we first assumed the completely textured grain orientations (*i.e.*, no variation of the grain orientations). For the overall composition, we also choose $u_0 = 0.17$. We choose the GB-solute interaction parameter $m_g^* = 3.0$ and the GB relaxation parameter $\rho = 0.0$ (no relaxation). Fig. 11(b) shows the simulated multivariant hydride microstructures in a polycrystal. For better visualization of the GB-hydride interactions, we overlapped the grain structure image on the hydride microstructure images. For the given conditions, both intragranular and intergranular hydrides are observed. As expected, the hydrides formed along GBs are observed as indicated by yellow dashed ovals in the figure in addition to homogeneously nucleated hydrides inside grains. To observe the impact of grain orientations in a polycrystal, we also performed a simulation incorporating a small variation in the orientations of individual grains with the ranges of $-(\pi/36) \leq \alpha_g \leq (\pi/36)$, $-(\pi/36) \leq \beta_g \leq (\pi/36)$, $-(\pi/72) \leq \gamma_g \leq (\pi/72)$, where α_g , β_g , γ_g are the Euler angles that characterize the grain orientations. As shown in Fig. 11(c), we could also observe populated hydride variant stacks at GBs. However, some grains exhibit non-stacking

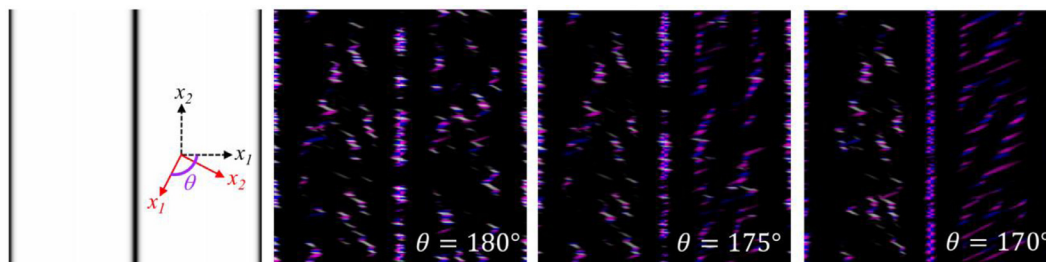


Fig. 10. Cross sections of simulated δ -hydrides (with mixed coherency $q = 0.82$) microstructures (at $t = 40,000\Delta t$) bi-crystals with grain rotation. White/blue/magenta represent variant 1/variant 2/variant 3. (For interpretation of the references to color in this figure legend, the reader is referred to the web version of this article.)

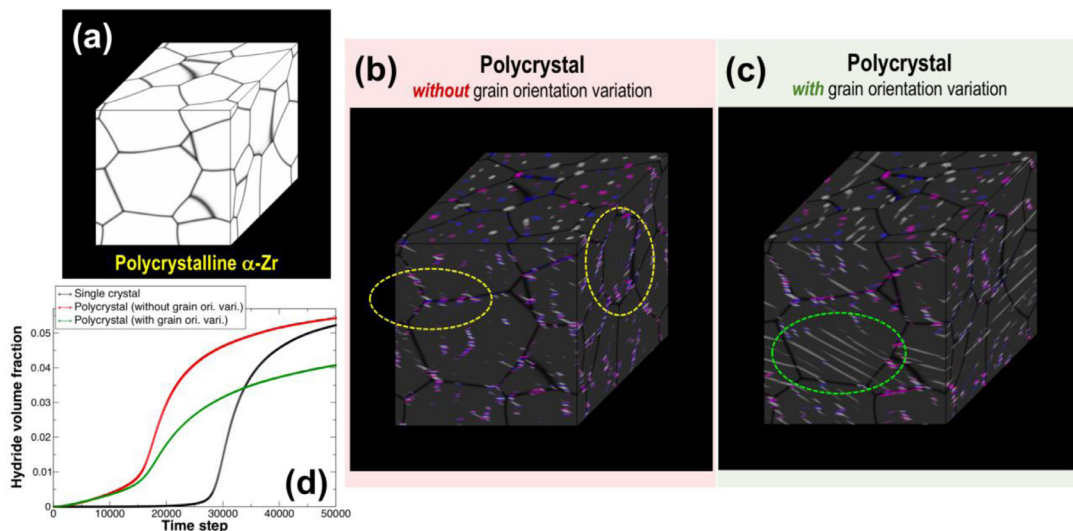


Fig. 11. (a) Prepared polycrystalline α -Zr for simulating δ -hydride formation; (b) Simulated δ -hydride microstructure in a polycrystal without grain orientation variation (at $t = 40,000\Delta t$); (c) Simulated δ -hydride microstructure in a polycrystal with grain orientation variation ($t = 40,000\Delta t$); and (d) Hydride volume fraction as a function of time for single and polycrystals. White/blue/magenta represent variant 1/variant 2/variant 3 in (b) and (c). (For interpretation of the references to color in this figure legend, the reader is referred to the web version of this article.)

behaviors of hydrides (highlighted in a green dashed oval in the figure). Similar to the bi-crystal case with a rotated grain, those grains are expected to be under the internal shear stress exerted by the natural mechanical constraint established by neighboring grains containing volume expansion due to hydride formation. We note that qualitatively similar types of various GB-hydride interactions have been experimentally characterized for a hydrided polycrystalline Zr alloy [90].

To compare hydride formation in polycrystals with the single crystal counterpart, we monitor the hydride volume fraction, which was measured by a criterion $\eta \geq 0.45$, as a function of time. Fig. 11(d) explicitly shows that the hydride formation kinetics at early stages in both cases of polycrystals are faster than in the single crystal case. This can be easily understood by the early nucleation of GB hydrides mediated by GB segregation of hydrogen discussed above. Intriguingly, our simulations show that two polycrystals exhibit quite similar kinetics of the hydride volume fractions at early stages, while they become different in the later stages. In particular, for the polycrystal containing small variation of grain orientations, the hydride formation kinetics becomes slower compared to the polycrystal without the grain orientation variation. It may be understood by the fact that the early stages are governed by the GB nucleated hydride formation for which both polycrystals have same amount of heterogeneous nucleation sites (or GB area). However, the later stages are governed by the kinetics of growth of already nucleated hydrides at GB as well as intragranular nucleation-and-growth of hydrides. Both processes can be affected by the long-range internal stress field

[53] that is sensitive to the grain orientations and evolving phase microstructures. To support this argument, we also monitored the internal stress built up within the system upon hydrides formation. We chose the hydride microstructures in a single crystal and polycrystals with similar volume fractions of hydrides at later stages. We then evaluate the von Mises stress defined as: $\sigma_{vM} = \sqrt{(1/2)[(\sigma_{11} - \sigma_{22})^2 + (\sigma_{22} - \sigma_{33})^2 + (\sigma_{33} - \sigma_{11})^2 + 6(\sigma_{23}^2 + \sigma_{31}^2 + \sigma_{12}^2)]}$. The spatial profiles of the computed von Mises stress are shown in Fig. 12(a) for corresponding microstructures. The stress profiles clearly indicate that internal stresses are highly concentrated at or near hydrides. Our separate calculations (see the inset of Fig. 12(b)) of the local pressure ($= -(\sigma_{11} + \sigma_{22} + \sigma_{33})/3$) confirm that the formed hydrides are compressively stressed. This trend is consistent with available experimental observations using the x-ray synchrotron diffraction technique [64]. By analyzing the computed von Mises stress profiles, we obtained the statistics of the magnitudes of the von Mises stress over the entire system for the three microstructures. Fig. 12(b) includes the stress distributions for the single crystal and the two polycrystals. The distribution for the polycrystal with the grain orientation variation exhibits the notable difference from the distributions of other two cases. As we discussed above, this may be the reason for the different volume fraction kinetic behavior at later stages of hydride formation in the polycrystal with the grain orientation variation (see Fig. 11(d)). Moreover, the similar stress distributions of the single crystal and the perfectly textured polycrystal (with no grain orientation variation) cases may explain the similar

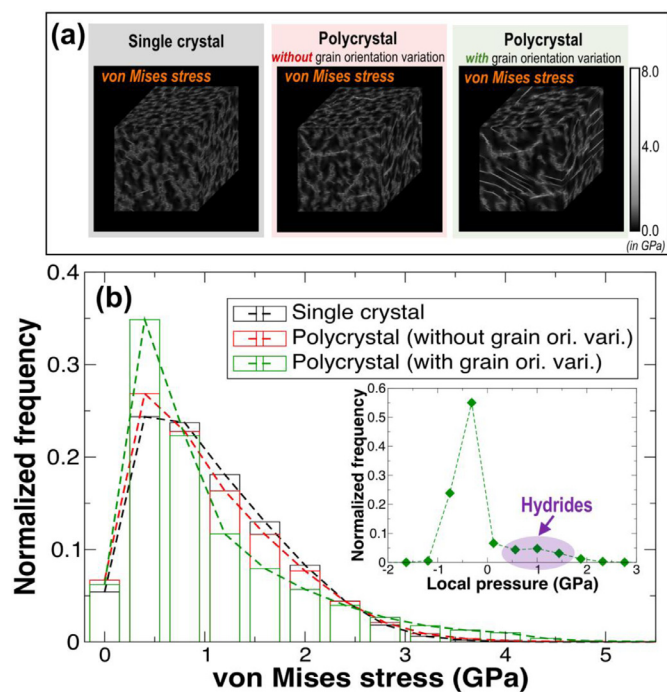


Fig. 12. (a) Computed von Mises stress profiles for single crystal and polycrystals containing similar volume fractions of formed hydrides; and (b) Statistical von Mises stress distributions over entire systems for the three cases (inset: statistics of computed local pressures).

slopes of the volume fraction curves at later stages for the two cases in Fig. 11(d). Note that those slopes at later stages in both cases are dominated by the homogeneous nucleation-and-growth of hydrides, of which the kinetic barrier involves more significant internal stresses. Therefore, our simulations for polycrystalline α -Zr verify that the hydride formation kinetics is highly sensitive to the grain texture and the associated internal stress due to formation of hydrides themselves.

4. Summary

In this study, a comprehensive phase-field model was developed for investigating hydride formation and their morphologies involving large volume expansion in single and polycrystalline metals employing the δ -hydride formation in α -Zr as a model system. Consequently, we emphasize three novel features of our model and simulation study. First, we successfully implemented key necessary modeling factors for modeling hydride formation in polycrystalline metals within the phase-field framework, including the thermodynamic free energy functions based on the sublattice model and CALPHAD database, the phase-dependent diffusivities of hydrogen, the hydrogen-GB interaction, and the inhomogeneous elasticity for the two-phase multivariant polycrystal. Second, we introduced the *mixed interfacial coherency* concept for deriving the stress-free transformation strains for hydride variants involving large volume expansion. Third, our devised model allows for a parametric simulation study, by which we could add new insight into hydride microstructure formation mechanisms associated with the interfacial coherency variation and hydride-grain boundary interactions. We performed computer simulations, which qualitatively captured several of experimentally characterized hydride microstructural features including stacking behaviors and interactions with grain boundaries [90] (see Fig. S4 in Supplemental material S6 for example).

More specifically, the model permitted performing controlled simulations for exploring the morphological (in)stability of multivariant hydrides upon interfacial coherency variation. This behavior was explained by referring to the identified habit plane modes for the different coherency states. We also carried out phase-field simulations incorporating random fluctuations of field variables to observe the behaviors of naturally nucleated δ -hydrides in single- and bi-crystals of α -Zr. By analyzing our phase-field simulation results, we propose three possible hydride re-orientation mechanisms:

- **Mechanism 1:** The applied load may induce structural defects at hydride/metal interfaces, which cause interfacial coherency loss along the c -axis. The corresponding coherency state variation affects the growth direction of individual hydride variants and eventually enhances hydride stacking behavior, leading to the effective growth of the macro-platelets of the hydrides more aligned along the c -axis.
- **Mechanism 2:** The possible shear component of the applied stress, which may arise from grain texture or sample geometry, causes the selection of certain variants of hydrides due to interactions between the shear stress and the shear component of the transformation strain. This variant selection behavior coupled with coherency loss along the c -axis induces more compact stacking behaviors of the selected variants, resulting in the growth of the macro-platelets more aligned along the c -axis.
- **Mechanism 3:** Individual hydride variants with fully coherent hydride/metal interfaces tend to independently grow and be more aligned along the basal plane. These fully coherent variants interact more strongly with and segregate to grain boundaries aligned along the basal plane. On the other hand, according to the proposed Mechanism 1, the coherency loss along the c -axis enhances the stacking tendency of the hydride variants, leading to the growth of the macro-platelet aligned along the c -axis. These macro-platelets tend to segregate at grain boundaries aligned along the c -axis. Therefore, the re-orientation tendency due to coherency loss is enhanced by those hydride-grain boundary interaction behaviors.

The developed model can also be employed to simulate the hydride formation in generic polycrystalline α -Zr containing multiple grains. Our simulations demonstrated that the kinetics of hydride formation is strongly affected by the grain texture and the internal stress arising from the precipitated hydrides themselves.

Our present model is comprehensively descriptive in terms of operating physical factors that determine the hydride microstructural features. On the other hand, our approach includes a few limitations, which require further development for the better predictive capability of the model. First, our current phase-field model incorporating new concepts carries additional free parameters such as the misfit parameter q . Although we performed parametric simulation studies for those parameters, more detailed experimental verification is required to further refine the concepts. Second, the mechanical equilibrium and coherency strain energy formalisms are based on the linear elasticity theory, although the stress-free transformation strain involving large volume expansion is based on the nonlinear (finite strain) theory. Our model can be extended by implementing the entirely nonlinear self-consistent elasticity formalism for polycrystals in the context of the phase-field microelasticity framework. Third, we assume the static misfit parameter q during formation and growth of the hydride phase. The model for the misfit parameter can be refined by introducing the mechanisms for the natural onset of interfacial coherency loss and the variation of the coherency state in response to applied loads or local stresses/strains. This may require a proper model that takes into account creation or activity of interfacial defects (e.g., dislocations) based on the constitutive laws for plasticity. Fourth, our

model ignores the impacts of interfacial defects on the energetics for simplicity. In particular, the interfacial energy can vary depending on the interfacial defect density [91]. The model for the gradient energy coefficients can be extended to include their misfit parameter-dependences.

We emphasize that this proposed comprehensive modeling framework is generally applicable to phase transformations involving diffusional processes, crystallographic structural changes, and large volume expansion in many other materials systems.

Acknowledgments

The work of T.W. Heo was performed under the auspices of the U.S. Department of Energy by Lawrence Livermore National Laboratory (LLNL) under Contract DE-AC52-07NA27344. This work was partially funded by the Laboratory Directed Research and Development Program at LLNL under a project tracking code 18-SI-001. This work is also partially funded by support through the Hydrogen Materials – Advanced Research Consortium (HyMARC) of the U.S. Department of Energy (DOE), Office of Energy Efficiency and Renewable Energy (EERE), Fuel Cell Technologies Office (FCTO) under Contract DE-AC52-07NA27344. The work of K.B. Colas and A.T. Motta was supported by the Materials World Network Grant DMR-0710616 from the National Science Foundation. L.Q. Chen is partially supported by the DOE NEUP Integrated Research Project IRP-17-13708. Additional computing support came from the LLNL Institutional Computing Grand Challenge program. Helpful discussions about metal/hydrides interfaces with Dr. B.C. Wood (LLNL) and Dr. S. Kang (LLNL) and about general concepts of hydriding-dehydriding of materials with Dr. J.R. Jeffries (LLNL) and Dr. K.S. Holliday (LLNL) are acknowledged. The views and opinions of the authors expressed herein do not necessarily state or reflect those of the United States Government or any agency thereof. Neither the United States Government nor any agency thereof, nor any of their employees, makes any warranty, expressed or implied, or assumes any legal liability or responsibility for the accuracy, completeness, or usefulness of any information, apparatus, product, or process disclosed, or represents that its use would not infringe privately owned rights.

Supplementary materials

Supplementary material associated with this article can be found, in the online version, at doi:10.1016/j.actamat.2019.09.047.

References

- [1] V. Bérubé, G. Radtke, M. Dresselhaus, G. Chen, Size effects on the hydrogen storage properties of nanostructured metal hydrides: a review, *Int. J. Energy Res.* 31 (6–7) (2007) 637–663.
- [2] L.E. Klebanoff, J.O. Keller, 5 Years of hydrogen storage research in the US DOE metal hydride center of excellence (MHCoE), *Int. J. Hydrogen Energy* 38 (11) (2013) 4533–4576.
- [3] A. Schneemann, J.L. White, S. Kang, S. Jeong, L.W.F. Wan, E.S. Cho, T.W. Heo, D. Prendergast, J.J. Urban, B.C. Wood, M.D. Allendorf, V. Stavila, Nanostructured metal hydrides for hydrogen storage, *Chem. Rev.* 118 (22) (2018) 10775–10839.
- [4] M. Blat, L. Legras, D. Noel, H. Amanrich, Contribution to a better understanding of the detrimental role of hydrogen on the corrosion rate of Zircaloy-4 cladding materials, ASTM, Zirconium in the Nuclear Industry: Twelfth International Symposium, 1354, ASTM, STP, 2000, pp. 563–591.
- [5] V. Bhosle, E.G. Baburaj, M. Miranova, K. Salama, Dehydrogenation of TiH₂, *Mater. Sci. Eng. A – Struct. Mater. Prop. Microstruct. Process.* 356 (1–2) (2003) 190–199.
- [6] D.Y. Kovalev, V.K. Prokudina, V.I. Ratnikov, V.I. Ponomarev, Thermal decomposition of TiH₂: a TRXRD study, *Int. J. Self-Propagating High-Temp. Synth.* 19 (4) (2010) 253–257.
- [7] J.M. Joubert, Calphad modeling of metal–hydrogen systems: a review, *JOM* 64 (12) (2012) 1438–1447.
- [8] Y. Pang, Q. Li, A review on kinetic models and corresponding analysis methods for hydrogen storage materials, *Int. J. Hydrogen Energy* 41 (40) (2016) 18072–18087.
- [9] X.W. Zhou, T.W. Heo, B.C. Wood, V. Stavila, S. Kang, M.D. Allendorf, Temperature- and concentration-dependent hydrogen diffusivity in palladium from statistically-averaged molecular dynamics simulations, *Scr. Mater.* 149 (2018) 103–107.
- [10] Y.F. Zhang, C. Jiang, X.M. Bai, Anisotropic hydrogen diffusion in alpha-Zr and Zircaloy predicted by accelerated kinetic Monte Carlo simulations, *Sci. Rep.* 7 (2017) 13.
- [11] A.V. Yanilkin, Quantum molecular dynamics simulation of hydrogen diffusion in zirconium hydride, *Phys. Solid State* 56 (9) (2014) 1879–1885.
- [12] A. Gross, Ab initio molecular dynamics simulations of the adsorption of H-2 on palladium surfaces, *ChemPhysChem* 11 (7) (2010) 1374–1381.
- [13] M. Pozzo, D. Alfe, A. Amieiro, S. French, A. Pratt, Hydrogen dissociation and diffusion on Ni- and Ti-doped Mg(0001) surfaces, *J. Chem. Phys.* 128 (9) (2008) 11.
- [14] S.R. de Debiaggi, E.A. Crespo, F.U. Braschi, E.M. Bringa, M.L. Ali, M. Ruda, Hydrogen absorption in Pd thin-films, *Int. J. Hydrogen Energy* 39 (16) (2014) 8590–8595.
- [15] N. Goldman, B. Aradi, R.K. Lindsey, L.E. Fried, Development of a multicenter density functional tight binding model for plutonium surface hydriding, *J. Chem. Theory Comput.* 14 (5) (2018) 2652–2660.
- [16] J.J. Tang, X.B. Yang, L.J. Chen, Y.J. Zhao, Modeling and stabilities of Mg/MgH₂ interfaces: a first-principles investigation, *AIP Adv.* 4 (7) (2014) 15.
- [17] S. Kang, T. Ogitsu, S.A. Bonev, T.W. Heo, M.D. Allendorf, B.C. Wood, Understanding charge transfer at Mg/MgH₂ interfaces for hydrogen storage, in: *Proceedings of Symposium on Solid-Gas Electrochemical Interfaces 2 (SGEI 2)*, 77, 2017, pp. 81–90.
- [18] M.A. Louchez, R. Besson, L. Thuinet, A. Legris, Interfacial properties of hydrides in alpha-Zr: a theoretical study, *J. Phys. – Condensed Matter* 29 (41) (2017) 14.
- [19] A. Pundt, R. Kirchheim, Hydrogen in metals: microstructural aspects, *Annu. Rev. Mater. Res.* 36 (1) (2006) 555–608.
- [20] K.J. Michel, V. Ozolins, Theory of mass transport in sodium alanate, *J. Mater. Chem. A* 2 (12) (2014) 4438–4448.
- [21] L.Q. Chen, Phase-field models for microstructure evolution, *Annu. Rev. Mater. Res.* 32 (2002) 113–140.
- [22] W.J. Boettinger, J.A. Warren, C. Beckermann, A. Karma, Phase-field simulation of solidification, *Annu. Rev. Mater. Res.* 32 (2002) 163–194.
- [23] L. Granasy, T. Pusztai, T. Borzsonyi, G. Toth, G. Tegze, J.A. Warren, J.F. Douglas, Phase field theory of crystal nucleation and polycrystalline growth: a review, *J. Mater. Res.* 21 (2) (2006) 309–319.
- [24] H. Emmerich, Advances of and by phase-field modelling in condensed-matter physics, *Adv. Phys.* 57 (1) (2008) 1–87.
- [25] N. Moelans, B. Blanpain, P. Wollants, An introduction to phase-field modeling of microstructure evolution, *Calphad – Comput. Coupling Phase Diagr. Thermochem.* 32 (2) (2008) 268–294.
- [26] I. Steinbach, Phase-field models in materials science, *Model. Simul. Mater. Sci. Eng.* 17 (7) (2009) 073001.
- [27] J.W. Cahn, J.E. Hilliard, Free energy of a nonuniform system. I. Interfacial free energy, *J. Chem. Phys.* 28 (2) (1958) 258–267.
- [28] A.T. Motta, L.Q. Chen, Hydride formation in zirconium alloys, *JOM* 64 (12) (2012) 1403–1408.
- [29] R.S. Daum, S. Majumdar, D.W. Bates, A.T. Motta, D.A. Koss, M.C. Billone, On the embrittlement of Zircaloy-4 under RIA-relevant conditions, ASTM, Zirconium in the Nuclear Industry: Thirteenth International Symposium, 1423, ASTM, STP, 2002, pp. 702–718.
- [30] R.S. Daum, S. Majumdar, Y. Liu, M.C. Billone, Radial-hydride embrittlement of high-burnup Zircaloy-4 fuel cladding, *J. Nucl. Sci. Technol.* 43 (9) (2006) 1054–1067.
- [31] K.B. Colas, A.T. Motta, J.D. Almer, M.R. Daymond, M. Kerr, A.D. Banchik, P. Vizcaino, J.R. Santisteban, In situ study of hydride precipitation kinetics and re-orientation in Zircaloy using synchrotron radiation, *Acta Mater.* 58 (20) (2010) 6575–6583.
- [32] C.E. Ells, Hydride precipitates in zirconium alloys (a review), *J. Nucl. Mater.* 28 (2) (1968) 129.
- [33] J.J. Kearns, C.R. Woods, Effect of texture grain size and cold work on precipitation of oriented hydrides in Zircaloy tubing and plate, *J. Nucl. Mater.* 20 (3) (1966) 241.
- [34] X.Q. Ma, S.Q. Shi, C.H. Woo, L.Q. Chen, Effect of applied load on nucleation and growth of gamma-hydrides in zirconium, *Comput. Mater. Sci.* 23 (1–4) (2002) 283–290.
- [35] X.Q. Ma, S.Q. Shi, C.H. Woo, L.Q. Chen, Phase-field simulation of hydride precipitation in bi-crystalline zirconium, *Scr. Mater.* 47 (4) (2002) 237–241.
- [36] X.Q. Ma, S.Q. Shi, C.H. Woo, L.Q. Chen, Simulation of gamma-hydride precipitation in bi-crystalline zirconium under uniformly applied load, *Mater. Sci. Eng. A – Struct. Mater. Prop. Microstruct. Process.* 334 (1–2) (2002) 6–10.
- [37] X.Q. Ma, S.Q. Shi, C.H. Woo, L.Q. Chen, The phase field model for hydrogen diffusion and gamma-hydride precipitation in zirconium under non-uniformly applied stress, *Mech. Mater.* 38 (1–2) (2006) 3–10.
- [38] X.H. Guo, S.Q. Shi, X.Q. Ma, Elastoplastic phase field model for microstructure evolution, *Appl. Phys. Lett.* 87 (22) (2005) 221910.
- [39] X.H. Guo, S.Q. Shi, Q.M. Zhang, X.Q. Ma, An elastoplastic phase-field model for the evolution of hydride precipitation in zirconium. Part I: smooth specimen, *J. Nucl. Mater.* 378 (1) (2008) 110–119.
- [40] X.H. Guo, S.Q. Shi, Q.M. Zhang, X.Q. Ma, An elastoplastic phase-field model for the evolution of hydride precipitation in zirconium. Part II: specimen with flaws, *J. Nucl. Mater.* 378 (1) (2008) 120–125.

- [41] L. Thuinet, A. De Backer, A. Legris, Phase-field modeling of precipitate evolution dynamics in elastically inhomogeneous low-symmetry systems: application to hydride precipitation in Zr, *Acta Mater.* 60 (13–14) (2012) 5311–5321.
- [42] L. Thuinet, A. Legris, L.F. Zhang, A. Ambard, Mesoscale modeling of coherent zirconium hydride precipitation under an applied stress, *J. Nucl. Mater.* 438 (1–3) (2013) 32–40.
- [43] S.Q. Shi, Z.H. Xiao, A quantitative phase field model for hydride precipitation in zirconium alloys: part I. Development of quantitative free energy functional, *J. Nucl. Mater.* 459 (2015) 323–329.
- [44] Z.H. Xiao, M.J. Hao, X.H. Guo, G.Y. Tang, S.Q. Shi, A quantitative phase field model for hydride precipitation in zirconium alloys: part II. Modeling of temperature dependent hydride precipitation, *J. Nucl. Mater.* 459 (2015) 330–338.
- [45] J. Bair, M.A. Zaeem, M. Tonks, A phase-field model to study the effects of temperature change on shape evolution of gamma-hydrides in zirconium, *J. Phys. D – Appl. Phys.* 49 (40) (2016) 10.
- [46] A.M. Jokisaari, K. Thornton, General method for incorporating Calphad free energies of mixing into phase field models: application to the alpha-zirconium/delta-hydride system, *Calphad – Comput. Coupling Phase Diagr. Thermochem.* 51 (2015) 334–343.
- [47] I. Steinbach, F. Pezzolla, B. Nestler, M. Seesselberg, R. Prieler, G.J. Schmitz, J.L.L. Rezende, A phase field concept for multiphase systems, *Physica D* 94 (3) (1996) 135–147.
- [48] J. Bair, M.A. Zaeem, D. Schwen, Formation path of delta hydrides in zirconium by multiphase field modeling, *Acta Mater.* 123 (2017) 235–244.
- [49] G.M. Han, Y.F. Zhao, C.B. Zhou, D.-Y. Lin, X.Y. Zhu, J. Zhang, S.Y. Hu, H.F. Song, Phase-field modeling of stacking structure formation and transition of δ -hydride precipitates in zirconium, *Acta Mater.* 165 (2019) 528–546.
- [50] J. Bair, M.A. Zaeem, M. Tonks, A review on hydride precipitation in zirconium alloys, *J. Nucl. Mater.* 466 (2015) 12–20.
- [51] A.T. Motta, L. Capolungo, L.Q. Chen, M.N. Cinbiz, M.R. Daymond, D.A. Koss, E. Lacroix, G. Pastore, P.C.A. Simon, M.R. Tonks, B.D. Wirth, M.A. Zikry, Hydrogen in zirconium alloys: a review, *J. Nucl. Mater.* 518 (2019) 440–460.
- [52] T.W. Heo, S. Bhattacharyya, L.Q. Chen, A phase-field model for elastically anisotropic polycrystalline binary solid solutions, *Philos. Mag.* 93 (13) (2013) 1468–1489.
- [53] T.W. Heo, L.Q. Chen, Phase-field modeling of displacive phase transformations in elastically anisotropic and inhomogeneous polycrystals, *Acta Mater.* 76 (2014) 68–81.
- [54] L.Q. Chen, Y.Z. Wang, A.G. Khachaturyan, Kinetics of tweed and twin formation during an ordering transition in a substitutional solid-solution, *Philos. Mag. Lett.* 65 (1) (1992) 15–23.
- [55] D. Fan, L.-Q. Chen, Computer simulation of twin formation during the displacive $c \rightarrow t'$ phase transformation in the zirconia-yttria system, *J. Am. Ceram. Soc.* 78 (3) (1995) 769–773.
- [56] Y. Wang, A.G. Khachaturyan, Three-dimensional field model and computer modeling of martensitic transformations, *Acta Mater.* 45 (2) (1997) 759–773.
- [57] Y.M. Jin, A. Artemev, A.G. Khachaturyan, Three-dimensional phase field model of low-symmetry martensitic transformation in polycrystal: simulation of zeta (ζ) martensite in AuCd alloys, *Acta Mater.* 49 (12) (2001) 2309–2320.
- [58] A. Artemev, Y. Jin, A.G. Khachaturyan, Three-dimensional phase field model of proper martensitic transformation, *Acta Mater.* 49 (7) (2001) 1165–1177.
- [59] Y.U. Wang, Y.M. Jin, A.G. Khachaturyan, Three-dimensional phase field microelasticity theory of a complex elastically inhomogeneous solid, *Appl. Phys. Lett.* 80 (24) (2002) 4513–4515.
- [60] S. Bhattacharyya, T.W. Heo, K. Chang, L.Q. Chen, A spectral iterative method for the computation of effective properties of elastically inhomogeneous polycrystals, *Commun. Comput. Phys.* 11 (3) (2012) 726–738.
- [61] T.W. Heo, S. Bhattacharyya, L.Q. Chen, A phase field study of strain energy effects on solute-grain boundary interactions, *Acta Mater.* 59 (20) (2011) 7800–7815.
- [62] K.B. Colas, A.T. Motta, M.R. Daymond, M. Kerr, J.D. Almer, Hydride platelet reorientation in Zircaloy studied with synchrotron radiation diffraction, *J. ASTM Int.* 8 (1) (2011) JA1103033 (17 pp.).
- [63] K.B. Colas, A.T. Motta, M.R. Daymond, J.D. Almer, Effect of thermo-mechanical cycling on zirconium hydride reorientation studied in situ with synchrotron X-ray diffraction, *J. Nucl. Mater.* 440 (1–3) (2013) 586–595.
- [64] K.B. Colas, A.T. Motta, M.R. Daymond, J.D. Almer, Mechanisms of hydride reorientation in Zircaloy-4 studied in situ, *ASTM, Zirconium in the Nuclear Industry: Seventeenth International Symposium*, 1543, ASTM, STP, 2015, pp. 1107–1137.
- [65] S.M. Allen, J.W. Cahn, Microscopic theory for antiphase boundary motion and its application to antiphase domain coarsening, *Acta Metall.* 27 (6) (1979) 1085–1095.
- [66] Y.F. Zhang, X.M. Bai, J.G. Yu, M.R. Tonks, M.J. Noordhoek, S.R. Phillpot, Homogeneous hydride formation path in alpha-Zr: molecular dynamics simulations with the charge-optimized many-body potential, *Acta Mater.* 111 (2016) 357–365.
- [67] S.G. Kim, W.T. Kim, T. Suzuki, Phase-field model for binary alloys, *Phys. Rev. E* 60 (6) (1999) 7186–7197.
- [68] B. Sundman, J. Agren, A regular solution model for phases with several components and sub-lattices, suitable for computer-applications, *J. Phys. Chem. Solids* 42 (4) (1981) 297–301.
- [69] N. Dupin, I. Ansara, C. Servant, C. Toffolon, C. Lemaignan, J.C. Brachet, A thermodynamic database for zirconium alloys, *J. Nucl. Mater.* 275 (3) (1999) 287–295.
- [70] K. Gronhagen, J. Agren, Grain-boundary segregation and dynamic solute drag theory – a phase-field approach, *Acta Mater.* 55 (3) (2007) 955–960.
- [71] A.G. Khachaturyan, *Theory of Structural Transformations in Solids*, John Wiley & Sons, New York, 1983.
- [72] D.O. Northwood, R.W. Gilbert, Hydrides in zirconium-2.5 wt.-percent niobium alloy pressure tubing, *J. Nucl. Mater.* 78 (1) (1978) 112–116.
- [73] Y.H. Wen, L.Q. Chen, P.M. Hazzledine, Y. Wang, A three-dimensional phase-field model for computer simulation of lamellar structure formation in gamma TiAl intermetallic alloys, *Acta Mater.* 49 (12) (2001) 2341–2353.
- [74] V. Vaithyanathan, C. Wolverton, L.Q. Chen, Multiscale modeling of precipitate microstructure evolution, *Phys. Rev. Lett.* 88 (12) (2002) 4.
- [75] V. Vaithyanathan, C. Wolverton, L.Q. Chen, Multiscale modeling of theta (θ') precipitation in Al-Cu binary alloys, *Acta Mater.* 52 (10) (2004) 2973–2987.
- [76] T.W. Heo, M. Tang, L.Q. Chen, B.C. Wood, Defects, entropy, and the stabilization of alternative phase boundary orientations in battery electrode particles, *Adv. Energy Mater.* 6 (6) (2016) 10.
- [77] A. Artemev, Y.M. Jin, A.G. Khachaturyan, Three-dimensional phase field model and simulation of cubic \rightarrow tetragonal martensitic transformation in polycrystals, *Philos. Mag. A – Phys. Condensed Matter Struct. Defects Mechan. Prop.* 82 (6) (2002) 1249–1270.
- [78] J.W. Cahn, On spinodal decomposition, *Acta Metall.* 9 (9) (1961) 795–801.
- [79] G. Majer, W. Renz, R.G. Barnes, The mechanism of hydrogen diffusion in zirconium dihydrides, *J. Phys. – Condensed Matter* 6 (15) (1994) 2935–2942.
- [80] J.Z. Zhu, L.Q. Chen, J. Shen, V. Tikar, Coarsening kinetics from a variable-mobility Cahn-Hilliard equation: application of a semi-implicit Fourier spectral method, *Phys. Rev. E* 60 (4) (1999) 3564–3572.
- [81] L.Q. Chen, J. Shen, Applications of semi-implicit Fourier-spectral method to phase field equations, *Comput. Phys. Commun.* 108 (2–3) (1998) 147–158.
- [82] S.Y. Hu, L.Q. Chen, A phase-field model for evolving microstructures with strong elastic inhomogeneity, *Acta Mater.* 49 (11) (2001) 1879–1890.
- [83] P. Yu, S.Y. Hu, L.Q. Chen, Q. Du, An iterative-perturbation scheme for treating inhomogeneous elasticity in phase-field models, *J. Comput. Phys.* 208 (1) (2005) 34–50.
- [84] H.M. Chung, R.S. Daum, J.M. Hiller, M.C. Billone, Characteristics of hydride precipitation and reorientation in spent-fuel cladding, *ASTM, Zirconium in the Nuclear Industry: Thirteenth International Symposium*, 1423, ASTM, STP, 2002, pp. 561–580.
- [85] V.S. Arunacha, B. Lehtinen, G. Ostberg, Orientation of zirconium hydride on grain boundaries in Zircaloy-2, *J. Nucl. Mater.* 21 (3) (1967) 241.
- [86] N. Kumar, J.A. Szpunar, EBSD studies on microstructure and crystallographic orientation of delta-hydrides in Zircaloy-4, Zr-1% Nb and zr-2.5% Nb, *Mater. Sci. Eng. A – Struct. Mater. Prop. Microstruct. Process.* 528 (21) (2011) 6366–6374.
- [87] L.Q. Chen, W. Yang, Computer-simulation of the domain dynamics of a quenched system with a large number of nonconserved order parameters – the grain-growth kinetics, *Phys. Rev. B* 50 (21) (1994) 15752–15756.
- [88] C.E. Krill, L.Q. Chen, Computer simulation of 3-D grain growth using a phase-field model, *Acta Mater.* 50 (12) (2002) 3057–3073.
- [89] W. Qin, N. Kumar, J.A. Szpunar, J. Kozinski, Intergranular delta-hydride nucleation and orientation in zirconium alloys, *Acta Mater.* 59 (18) (2011) 7010–7021.
- [90] S.Y. Wang, F. Giuliani, T. Ben Britton, Microstructure and formation mechanisms of delta-hydrides in variable grain size Zircaloy-4 studied by electron backscatter diffraction, *Acta Mater.* 169 (2019) 76–87.
- [91] R. Shi, N. Ma, Y. Wang, Predicting equilibrium shape of precipitates as function of coherency state, *Acta Mater.* 60 (10) (2012) 4172–4184.